

A numerical study of microburst-like wind load acting on different block array configurations using an impinging jet model

Tze Siang Sim¹, Muk Chen Ong^{2,3}, Wee Yong Quek¹, Zheng Wei Sum¹, Wei Xian Lai¹, and Martin Skote^{*1}

¹School of Mechanical and Aerospace Engineering, Nanyang Technological University, 50 Nanyang Avenue, Singapore 639798

²Department of Mechanical and Structural Engineering and Materials Science, University of Stavanger, 4036 Stavanger, Norway

³Norwegian Marine Technology Research Institute (MARINTEK), NO-7450 Trondheim, Norway

Abstract. A numerical investigation on the microburst-like wind characteristics in block array configurations has been performed using Computational Fluid Dynamics (CFD). The CFD modelling of impinging jet mimics a microburst wind shear. Effects of plan and frontal area densities on the drag and lift force acting on the arrays are studied by investigating the wall shear stress and pressure distributions. A semi-empirical model based on Poreh *et al.* (1967) is derived to estimate the spatially-averaged wall shear stress of the finite urban array located near the microburst storm centre. Moreover, the pressure and viscous drag force acting on obstacles in the arrays with different plan and frontal area densities are discussed and compared with the published results regarding the arrays placed in a neutrally stratified Atmospheric Boundary Layer (ABL) flow. The present results show that the viscous drag is insignificant relative to the total drag force for all the cases with different frontal and plan area densities (i.e. roughness packing densities). The mean vertical lift force acting on the arrays for various packing densities are discussed, and the lift force is compared with drag and resultant forces. The averaged lift force acting on a block in the array is 0.3 – 0.6 times of the magnitude of the resultant force. Therefore, it should be taken into account for the design and maintenance of high-rise buildings in cities.

Keywords: CFD (computational fluid dynamics); dry microburst; array; obstacles; wind load effect

1. Introduction

Thunderstorm downburst is an intense transient downdraft of air that induces an outburst of extreme wind near the surface of the Earth. Fujita (1985) defined a type of downburst, known as microburst, in which the outflow extends less than 4km along the Earth's surface. The diameter of the full-scale microburst is between 400m to 4km (Fujita, 1985). The

*Corresponding author.

Email address: MSKOTE@ntu.edu.sg

extreme wind event typically lasts from 5 to 30 minutes (Letchford et al., 2002), and the height H of the thunderstorm microburst cloud measured from the cloud base to the surface of the Earth is about: $0.75 < H/D < 7.5$ (Hjelmfelt, 1988), where D is the diameter of the downdraft (see Fig. 1 for the definition sketch). The speed of the microburst outflow can reach as high as 75m/s (Letchford et al., 2002).

In the past years, experimental studies were conducted to investigate the flow characteristics of microburst wind shear using steady continuous circular impinging jet model. The impinging jet model has been proven being effective to model the mean flow characteristics of microburst (Choi, 2004; Hjelmfelt, 1988). Mason et al. (2005) created a pulse jet experimental apparatus to produce the primary vortex at about Reynolds number $Re = U_{jet}D/\nu = 2.96 \times 10^5$ and $H/D = 1.7$, where U_{jet} is the initial speed of the pulse jet and D in this experiment is the diameter of the jet and H is the height above a flat surface at which the pulse jet is released. Wherever the primary vortex travelled to, it left a signature on the pressure. They reported that the pressure underwent a positive to negative transition at $r/D = 1$, where r is the radial distance from the centreline of downdraft. Sengupta and Sarkar (2008) investigated the flow characteristics at about $Re = 1.39 \times 10^5$ and 2.22×10^5 . They plotted the surface pressure coefficient distribution around the centre of the impinging jet at $Re = 1.39 \times 10^5$. Xu and Hangan (2008) studied the effects of scale, boundary and inlet conditions of the impinging jet simulator for the application of microburst for $Re = 2.3 \times 10^4 - 1.9 \times 10^5$ at $H/D = 1 - 4$ and for five different inflow turbulence characteristics.

Computational Fluid Dynamics (CFD) has been used for parametric studies of microburst flow characteristics. Due to the large domains considered, the full governing equations cannot be solved as in fluid flow investigations of small and simple geometries (Skote 2014), although the averaged equations can still be utilized together with a suitable turbulence model. Kim and Hangan (2007) investigated the macro-dynamics and Reynolds number dependency of the flow at $H/D = 4$ and at $Re = 2 \times 10^4$, 1×10^5 and 2×10^6 , using the Reynolds stress model (RSM). Reynolds number dependency, due to separation of boundary layer, of the mean and unsteady velocity field was observed. The maximum velocity increases and the boundary layer depth decreases as the Re increases, whereas the flow becomes more periodic. Mason et al. (2009) employed the two-dimensional URANS techniques to carry out parametric study of a full-scale downburst. They reported that by

increasing the aerodynamic roughness length, the maximum outflow intensity decreases and the height of the maximum velocity increases. In their numerical simulation, a neutral rough standard wall function was adopted. In passing we note that the term *micro* in this context refers to very different scales compared to those in microfluidics where downburst due to temperature gradients has also been studied, see e.g. Mårtensson et al. (2006).

Semi-empirical velocity models have been created to allow an estimation of the full-scale isolated stationary microburst's steady-state radial velocity profile. The models can be used for load estimation, i.e by integrating the dynamic pressure expressed in terms of radial velocity along the vertical direction until the height of the obstacles. Li et al. (2012) further improved the existing analytical velocity models published by Oseguera and Bowles (1988) and Vicroy (1991) which took the development of microburst boundary layer as a linear variation. However, the boundary layer growth has a non-linear variation, as reported by Li et al. (2012). The revised model proposed by Li et al. (2012) incorporated the non-linear growth of the microburst boundary layer.

Compared to the conventional Atmospheric Boundary Layer (ABL) wind as specified in ASCE7-05 (2005), Zhang *et al.* (2013) commented that the wind pressure of microburst near the downdraft centre is much higher than those of ABL. To create better wind-resistant designs for the buildings in microburst-prone areas, the study on the effect of wind load on structures is required. For high-rise buildings, even if catastrophic failure will not occur, knowledge about the wind load effect is required from the serviceability and the economic points of view (Zhang et al., 2014b).

There are several published experimental studies of microburst wind load on building-like structures. Chay and Letchford (2002) investigated the mean pressure distribution along the centreline of the cube immersed in the microburst simulator. They found that at $r/D = 1$, the windward pressure was significantly greater than those of conventional ABL flow. However, at $r/D > 1.5$, the windward pressure becomes relatively similar to those of ABL. They concluded that the load at $r/D > 1.5$ is less significant than the load at $r/D = 1$, from a wind load design perspective. Li and Ou (2012) studied the pressure load of a stationary microburst simulator acting on a prismatic building model. They found that the top surface experience significant load when the building is located under the centre of impinging jet.

When the model is placed at $r/D = 1$, the loadings on the windward surface are greater than other locations. They recommended that the $r/D = 1$ location should be given more attention in practical engineering of the downburst-prone areas. Zhang et al. (2014a) investigated the microburst wind load acting on low-rise building types with various geometrical shapes, namely a cubical building, a grain bin and two gable-roofed buildings. They reported that the maximum pressure was found at $r/D = 1$, where the maximum radial velocity is also found. Zhang et al. (2014b) studied the effect of microburst wind load acting on high-rise buildings. When the building was placed at $r/D \geq 1$, they discovered that the lower windward wall experienced a high positive pressure, while significant suction or negative pressure was found on the sidewalls.

Only a few numerical studies have been performed to investigate the microburst wind load acting on buildings. Nicholls et al. (1993) used a cloud model, known as Regional Atmospheric Modeling System. In their work, soundings from field measurement were taken as the input to compute the pressure and streamline contours around an isolated cubical building. Kim et al. (2007) used CFD techniques to investigate the structural loads of a high-rise building impacted by full-scale microburst wind. The microburst wind loads were investigated by changing the position of the building and the size of microburst. They reported that the microburst with diameter sizes larger than 2000m might produce governing design wind loads higher than those of conventional ABL for the same high-rise building.

Based on published literature, all existing works involve either an isolated building block or none. To the authors' knowledge, neither experimental nor numerical results are available in the open literature for the study on full-scale stationary microburst flow characteristics and wind load effect in an urban city. The objective of this paper is to study the microburst aerodynamic quantities, and wind load acting on several block array configurations. In this study, the obstacles in the array are simplified models of real-scale high-rise buildings. In 1999, the morphology of 11 sites in 7 North American cities had been quantified by the use of plan area density λ_P and frontal area density λ_F via Geographic Information Systems (GIS) surveys (Grimmond and Oke, 1999). Therefore, roughness packing densities (Grimmond and Oke, 1999; Theurer et al., 1992), namely λ_P and λ_F , will be used to quantify the array configurations herein. Thereafter, the influence of λ_P and λ_F on the drag force, wall shear stress and pressure distribution, as well as the lift force will be studied by considering the

effects of λ_P and λ_F on them. A predictive model for estimating the spatially-averaged wall shear stress of the arrays is also presented.

2. Numerical Method

2.1 Governing equations

Reynolds-averaged Navier-Stokes (RANS) model is chosen in this study due to its capability in modelling time-averaged flow characteristics and forces in fully turbulent jet impingement flow (Zuckerman and Lior, 2005) and in the flow around obstacles (Ong *et al.*, 2009; Skote *et al.*, 2005; Tian *et al.*, 2013). The RANS model is less costly and more time efficient than large-eddy simulation (LES) and direct numerical simulation (DNS). The RANS model consists of time-averaged instantaneous continuity and momentum equations, as shown in Eqs. (1)-(2), which are known as the Reynolds-averaged equations. Furthermore, the maximum microburst wind speed ever recorded on field measurement is 75m/s (Letchford *et al.*, 2002) (i.e. Mach number (Ma) less than 0.3), and thus the jet is incompressible. The incompressible RANS equations read:

$$\frac{\partial u_i}{\partial x_i} = 0 \quad (1)$$

$$\frac{\partial u_i}{\partial t} + u_j \frac{\partial u_i}{\partial x_j} = f_i - \frac{1}{\rho} \frac{\partial p}{\partial x_i} + \nu \frac{\partial^2 u_i}{\partial x_j \partial x_j} - \frac{\partial \langle u'_i u'_j \rangle}{\partial x_j} \quad (2)$$

where $u_{i,j}$, $i, j \in [1, 2, 3]$ denotes the time-averaged velocity component components in the streamwise (x_1), spanwise (x_2) and vertical (x_3) directions respectively; $(x_1, x_2, x_3) = (X, Y, Z)$; f_i is the time-averaged body force; $\langle u'_i u'_j \rangle$ is the Reynolds stress tensor where u'_i and u'_j are the fluctuating velocity components; ν is the kinematic viscosity of air; ρ is the density of air, and p is the time-averaged pressure. From our numerical investigation it is clear that the gravity term does not have a significant effect on the velocity and thus the pressure field. Hence, the gravity can be ignored.

The Reynolds stress tensor $\langle u'_i u'_j \rangle$ is determined by Boussinesq hypothesis in this study. The Boussinesq hypothesis in the two-equation turbulence models is the expression of the

Reynolds stress components in terms of strain rate tensor $S_{ij} = \frac{1}{2} \left(\frac{\partial u_j}{\partial x_i} + \frac{\partial u_i}{\partial x_j} \right)$, turbulent kinematic viscosity ν_T and turbulent kinetic energy k , as shown in Eq. (3):

$$\langle u'_i u'_j \rangle = -2S_{ij}\nu_T + \frac{2}{3}k\delta_{ij} \quad (3)$$

where δ_{ij} is the Kronecker's delta function.

2.2 Numerical simulation schemes, computational domain and boundary conditions

The OpenFOAM solver – simpleFoam (a finite volume CFD solver written in C++ using object oriented techniques (OpenFOAM, 2014)) is chosen to model the steady-state RANS equations in the present study. The chosen turbulence model is $k - \omega$ SST (Menter, 1994).

Semi-implicit method for pressure-linked equations (SIMPLE) algorithm (Ferziger and Peric, 2001) is used to solve both Eqs (1) and (2). The convection, laplacian and gradient terms are approximated by second-order schemes, namely Gauss limited linear, Gauss limited corrected and Gauss linear schemes respectively. The use of Gauss limited linear scheme, a Total Variation Diminishing (TVD) scheme with Sweby filter (Sweby, 1984), to discretise the convection term is recommended by Versteeg and Malalasekera (2007). This is because the TVD scheme is very stable, and is bounded. It is also as accurate as the third-order Quadratic Upstream Interpolation for Convective Kinematics (QUICK) scheme. These schemes consist of a standard finite volume discretisation of Gaussian integration which requires the interpolation of values from the cell centres to the face centres.

In this study, seven simulation cases will be performed. In all the simulation cases, the impinging jet model is used to model the microburst-like flow. However, the impinging jet model is only valid for the flow near the ground surface. Since the surface-mounted arrays are the focus of this study, the impinging jet model will be sufficient for the investigation. One of the cases does not have an array, while the rest contain an array each (see Table 1). The purpose of the case without the array is to validate the turbulence model, boundary

conditions and numerical schemes by comparing the present results with the published data. The cases with arrays are investigated to address the objective of the present study.

For the case without array (labelled as A1), the size of the impinging jet model ($Re = U_{jet}D/\nu = 20,000$, where $D = 38.1\text{mm}$ and $U_{jet} = 7.6\text{m/s}$, and $H/D = 2, 4$) is set to be the same according to one of Kim and Hangan (2007)'s steady-state RANS simulations with $Re = U_{jet}D/\nu = 2.0 \times 10^4$ and $H/D = 4$. The inflow boundary is located at the nozzle of the impinging jet. The top of the domain is measured $6D$ vertically from the nozzle. The nozzle is $H/D = 2, 4$ from the ground. The top, front, back, left and right face of domain are the pressure outlets. The boundary conditions for velocity (u_1, u_2, u_3), pressure p , k and ω are tabulated in Table 2. The computational domain is three-dimensional and is measured $20D$ (X) by $20D$ (Y) by $10D$ (Z), as shown in Fig. 2.

For the cases with arrays (labelled as S1, S2, S3, S4, S5 and S6), the arrays are made of numerous cuboidal obstacles arranged in a staggered layout (i.e. array S1 is used as example in Fig. 3), similar to those described in Coceal et al. (2006). The arrays are rectangular in shape when viewed from the top perspective. The dimensions of the obstacles and the inter-obstacle spacing are varied from array to array. These dimensions are defined in Fig. 4, and the values are summarised in Table 3. The roughness packing densities, λ_p and λ_F , are computed using Eqs. (4) – (5), according to how Padhra (2010) computed them.

$$\lambda_p = \frac{\overline{A_p}}{\overline{A_T}} = \frac{\overline{L_X} \overline{L_Y}}{\overline{D_X} \overline{D_Y}} \quad (4)$$

$$\lambda_F = \frac{\overline{A_F}}{\overline{A_T}} = \frac{\overline{z_H} \overline{L_Y}}{\overline{D_X} \overline{D_Y}} \quad (5)$$

For S1 to S3, the λ_p is fixed at 0.243, while the λ_F is varied from 0.118 to 0.347. Between S4 and S6, the λ_F is fixed at 0.084, with the λ_p being varied between 0.059 to 0.181. The height of each obstacle is fixed at 50m , which is the height of a typical high-rise buildings (Grimmond and Oke, 1999). Note that the number of obstacles in the array (specified in Table 3) varies according to their different sizes.

The upstream edge of the array forms is aligned along the plane $X = 0$ (see Fig. 5). At $r/D = 1$, 0° orientation angle, the maximum positive pressure is found at the windward wall of the building, thus constitutes a design load case (Zhang et al., 2014a). This implies that the distance from the centreline of downdraft to the upstream edge has to be fixed at $r/D = 1$ to observe the maximum positive pressure acting on the array. In this study, the variables X and r are related by: $X/D + 1 = r/D$. The centreline of array is also aligned with the Cartesian X -axis (see Fig. 5), while the centreline of impinging jet nozzle is separated from the upstream edge of the array by $r/D = 1$ (see Fig. 5). The Reynolds number and height of the inlet for the impinging jet in the cases with arrays are $Re = U_{jet}D/\nu = 2.42 \times 10^9$ (where $D = 500m$ and $U_{jet} = 75m/s$) and $H/D = 2$, which are equivalent to those of microburst in nature (i.e. $D = 400m - 4,000m$; $U_{jet} = 75m/s$; $H/D = 0.75 - 7.5$ (Zhang, 2013)). The size of the computational domain in these cases with array is $20.5D$ (X) by $22D$ (Y) by $3D$ (Z). The inflow boundary is located at the nozzle of the impinging jet. The top of the domain is measured $1D$ vertically from the nozzle. The top, front, back, left and right domain patches are the pressure outlets. The size of all arrays is about $4.68D$ (X) by $2D$ (Y). The horizontal distances from the array to the outlets range is about $5.6D$ to $10D$, which have been checked carefully that the distance from the array to the outlets is far enough to eliminate the effects of the outlet boundaries. The boundary conditions for velocity (u_1, u_2, u_3), pressure p , k and ω are shown in Table 4.

The turbulence quantities ($k_{inlet}, \omega_{inlet}$) at the nozzle are calculated by Eqs. (6) – (7).

$$k_{inlet} = \frac{3}{2}(T.I \times U_{jet})^2 \quad (6)$$

$$\omega_{inlet} = k_{inlet}^{0.5}/(0.07 \times D \times C_\mu^{0.25}) \quad (7)$$

where $C_\mu = 0.09$ and $T.I$ is the turbulence intensity.

According to Viskanta (1993), an isothermal axisymmetric impinging jet turns fully turbulent at $Re > 3,000$. Hence the standard wall function can be applied at the near-wall region, around $y^+ \approx 30 - 40$, in all the present cases. The suitability of using standard wall function is also backed by Zhang (2013) and Mason *et al.* (2009)'s studies, in which standard

wall function produced results that were in good agreement with those of published field measurements, semi-empirical models and numerical simulations.

The turbulence quantities (k_{wall} , ω_{wall}) at the ground and array are calculated by Eqs. (8) – (9):

$$k_{\text{wall}} = \frac{3}{2} (T.I \times U_{\text{jet}})^2 \quad (8)$$

$$\omega_{\text{wall}} = k_{\text{wall}}^{0.5} / (0.07 \times D \times C_{\mu}^{0.25}) \quad (9)$$

The wall function for ω (see Eqs (10)) consists of a viscous sublayer component and log-law component, where y is the wall-normal distance and the von Kármán constant κ is equal to 0.41.

$$\omega = \sqrt{\left[\frac{6\nu}{\beta_1(y^2)} \Big|_{\text{vis}} \right]^2 + \left[\frac{\sqrt{k}}{C_{\mu}^{0.25} \kappa(y)} \Big|_{\text{log}} \right]^2} \quad (10)$$

The velocity flow in the log-law region is modelled using

$$u^+ = \frac{1}{\kappa} \ln(Ey^+) \quad (11)$$

where $y^+ = yu^*/\nu$ is the non-dimensional wall-adjacent node, $u^+ = u_{\text{tan}}/u_{\tau}$, u_{tan} is the tangential velocity to the wall, y is the wall-adjacent node distance, u^* is the effective friction velocity, and u_{τ} is the friction velocity. The value of $E = 9.793$ in Eq. (11) is the empirical constant for a smooth wall (Blocken *et al.*, 2007).

2.3 Grid-independence test

The grid-independence test is performed for the cases with array and without arrays. For case without array A1, the normalised radial velocity magnitude $|U_{\text{peak}}|/U_{\text{jet}}$ at $X/D = 1$ is used to differentiate the mesh quality. The examples of the mesh in case A1 are shown in Fig. 6. The mesh cases of A1 are labelled 1 to 3 in Table 5 with case 1 having the least cells and

case 3 the most cells. The difference in the number of cells between consecutive meshes (i.e mesh 1 versus mesh 2; mesh 2 versus mesh 3) are about 50%. To determine the relative difference in the computed $|U_{\text{peak}}|/U_{\text{jet}}$ of a particular mesh, mesh 1 is set as the reference for mesh 2 and mesh 3. In order to ensure that the differences in $|U_{\text{peak}}|/U_{\text{jet}}$ is not attributed to the iterations and the numerical schemes used, all the mesh cases are fixed to the same iterations and numerical schemes. The iterations required to obtain converged solutions is determined from a preliminary test involving the mesh 3 which has the most cells, since mesh 3 is expected to take the most iterations to converge the solution than meshes with less cells. It was found that the number of iterations required was close to 25,000. The outcome of the grid independent study of A1 shows that there is insignificant difference between the three cases (see Table 5). However, mesh 1 with the least number of cells is chosen, by virtue of the number of cells.

For the cases with arrays, the time-averaged total drag coefficient C_D is used to differentiate the results in the grid independent study. The S5 array is used as an example to show the mesh structures around the obstacles in Figs.7(a) and 7(b). The drag coefficient C_D is defined as follows:

$$C_D = \frac{D}{\frac{1}{2} \rho U_{\text{jet}}^2 A} \quad (12)$$

where D is the streamwise total drag force acting on the array and A is the projected frontal area of the array. The C_D for different array cases are tabulated in Table 6. For each array configuration, two different meshes, labelled 1 and 2, are compared. The difference in their cells between consecutive meshes (i.e mesh 1 versus mesh 2) is close to 50% of mesh 1 (i.e. mesh 1 has less cells than mesh 2), which is assigned to be the reference. Similar to the grid independent study of A1, the iterations required is determined separately from prior preliminary test using mesh 2 which has more cells than mesh 1. It was found that close to 100,000 iterations is required to ensure converged solutions in all the meshes. The outcome of the grid independent study on S1, S2, S3, S4, S5 and S6 shows that there is insignificant difference between the meshes 1 and 2 (see Table 6). However, mesh 1 with fewer cells is more preferred over mesh 2.

2.4 Discussions on numerical errors

It is expected that ABL wind engineering CFD simulation has at least a tolerance of 10^{-5} , according to guidelines (Franke et al., 2004; Schatzmann et al., 2010). Since OpenFoam RANS is commonly used for ABL wind engineering, it can be inferred that the tolerance of OpenFOAM RANS, which is used in the present study, will also have a tolerance limit of 10^{-5} at least.

3. Results and discussion

3.1 Case without array – validation of turbulence model and numerical setup

The results of A1 are discussed in this section. Fig. 8 shows the comparison of the vertical profile of the radial velocity profile at $r/D = 1$ between the present results and published results from microburst field measurements (Fujita, 1981; Hjelmfelt, 1988), experimental measurements (Mason *et al.*, 2005; Sengupta and Sarkar, 2008; Zhang, 2013), and semi-empirical models (Oseguera and Bowles, 1988; Vicroy, 1991; Wood *et al.*, 2001). The present result is found to be within the range of the published results. Fig. 9 shows the comparison of the radial velocity profiles at four radial locations $r/D = 1, 1.4, 2$ and 2.5 close to the stagnation region between the present results (at $Re = 20,000; H/D = 4$) and the published RANS results obtained by Kim and Hangan (2007) (at $Re = 20,000; H/D = 4$), as well as published experimental results from Hangan and Xu (2005) (at $Re = 27,000; H/D = 4$). The radial locations at $r/D = 1, 1.4, 2$ and 2.5 are chosen because within $r/D < 3$, the fluid quantities change very rapidly (Cooper *et al.*, 1993), and hence most studies associated with microburst wind engineering chose to focus within $r/D < 3$. The present results show close agreement with those of Kim and Hangan (2007)'s numerical results ($Re = 20,000; H/D = 4$) and the experimental results from Hangan and Xu (2005) ($Re = 27,000; H/D = 4$) at locations $r/D = 1, 1.4, 2$ and 2.5 . Even though Kim and Hangan (2007) had used a different turbulent model (i.e. Reynolds stress model (RSM)), together with the enhanced wall treatment that resolve the near-wall flow down to $y^+ \approx 1$, the present modelling is still able to predict the profile below the peak velocity at locations $r/D = 1, r/D = 1.4, r/D = 2$ and $r/D = 2.5$ with relatively good accuracy compared to those using the RSM model. Hangan and Xu (2005)'s experiment is chosen for comparison with the

present results as the order of magnitude of their Reynolds number is the same (i.e. $\sim O(10^4)$) as that of the present simulation and the one by Kim and Hangan (2007). Small discrepancies are observed between the present results and the experimental data by Hangan and Xu (2005). This is because even though the order of magnitude of Reynolds number is the same (i. e. $Re \sim O(10^4)$), the exact Reynolds numbers of the present results and of Hangan and Xu (2005)'s experiment are not identical. According to Xu and Hangan (2008), Reynolds number effect dominates for $Re < 27,000$, and this explains the slight deviation between the present results and the experimental data observed in the Fig. 9. Overall, the radial velocity within $r/D < 3$ is well predicted in this study. This implies that that the $k - \omega$ SST is capable of modelling the impinging jet flow. The choice of turbulence model is also consistent with the open literature findings that the $k - \omega$ SST model, together with standard wall functions, is able to perform well for impinging jet flow near the surface (Mason *et al.*, 2009).

3.2 Effects of frontal area density and plan area density on C_D

Three frontal area densities λ_F , referring to S1, S2 and S3 as shown in Table 3, are chosen to study their influence of the array configurations on C_D , while λ_P is fixed at 0.243. In the study of ABL flow over arrays, λ_F has been used to characterise the mutual sheltering effect of obstacles on drag (Shao and Yang, 2005). Shao and Yang (2005) suggested that the total drag due to ABL flow acting on the obstacles in the array should be partitioned into three components: a pressure drag, skin drag due to momentum transfer to the surfaces of obstacles and a surface drag due to momentum transfer to the ground. The effects of λ_F on the momentum transfer were studied. They concluded that, at small λ_F , the obstacles in the array should be treated as isolated obstacles and the mutual sheltering effect is not significant, thus the obstacles will increase the momentum transfer. In addition, as the λ_F increases, the mutual interference among obstacles leads to a decrease in momentum transfer.

Fig. 10 shows a decreasing trend in the C_D as λ_F increases while λ_P is fixed at 0.243. Between S3 and S2, λ_F is increased from 0.118 to 0.176 (by about 49.2%), and C_D is decreased from 0.68 to 0.65 (approximately -5.0%). Between S2 and S1, λ_F is increased from 0.176 to 0.347 (by about 97.2%), while C_D is decreased from 0.65 to 0.60 approximately (by

about -7.9%). The decreasing trend of C_D could possibly be due to the mutual sheltering effect as reported by Shao and Yang (2005).

Three plan area densities λ_p , referring to S4, S5 and S6 as shown in Table 3, are chosen to study the influence on C_D in Fig. 11, while λ_F is fixed at 0.084. Similar to λ_F , the λ_p can be used to characterise the mutual sheltering effect of obstacles on drag (Grimmond and Oke, 1999). Nonetheless, the investigated values of λ_p in the present study is limited to the range $0.059 \leq \lambda_p \leq 0.181$, in which the C_D increases as λ_p increases, while λ_F is fixed at 0.084. The trend is largely similar to those of neutrally-stratified ABL flow over a staggered array with density in the range $0.059 \leq \lambda_p \leq 0.181$ (Padhra, 2010). In addition, according to a DNS study of neutrally-stratified ABL flow over staggered array with similar packing density around $0.04 \leq \lambda_p \leq 0.25$ (Leonardi and Castro, 2010), the maximal surface drag under the ABL wind condition is reported to occur around $\lambda_p = 0.15$. For $\lambda_p < 0.15$, the values of surface drag increases with λ_p under ABL wind condition. Thus, the trend in the present study is largely similar to those of ABL wind condition, in the sense that both types of wind condition can cause the total drag force to increase within $\lambda_p < 0.15$. Furthermore, it can be inferred from the present trend of C_D that the mutual sheltering effect of obstacles is not dominant within the tested range of λ_p , since C_D is not decreasing with increasing λ_p for $0.059 \leq \lambda_p \leq 0.181$ and $\lambda_F = 0.084$ in the present study.

3.3 Effects of plan and frontal area density on the wall shear stress along the centreline of array

The total drag force around the array as microburst passes through is made up of two components, i.e. viscous drag and pressure drag. The viscous drag is due to wall shear stress acting on the wetted surfaces of the obstacles. According to Phares et al. (2000), a circular impinging jet flow can be divided into four flow zones: the free-jet region, the inviscid impingement region, the laminar impingement boundary layer region and the turbulent wall jet region. The total wall shear stress τ of the laminar impingement region is given by (Phares et al., 2000).

$$\frac{\tau}{\rho U_{jet}^2} Re^{0.5} \left(\frac{H}{D}\right)^2 = g\left(\frac{r}{H}\right) \quad (13)$$

where g is a universal function, but the exact expression is not provided by Phares et al. (2000). This model was developed based on laminar flow boundary layer theory, where the theory is valid near the stagnation region as the strong favourable pressure gradients suppress the turbulence near the ground. The flow at the impingement region is forced to behave like laminar flow.

The laminar boundary layer at certain radial location from the centre of the impingement zone undergoes a transition and turns into a turbulent axisymmetric radial wall jet, in which the spatial distribution of τ is described by Poreh *et al.* (1967) model.

$$\frac{\tau}{\rho U_{\text{jet}}^2} \text{Re}^{0.5} \left(\frac{H}{D}\right)^2 = 0.34 \text{Re}^{0.2} \left(\frac{r}{H}\right)^{-2.3} \quad (14)$$

It is observed that S1 and S4, Fig. 12 follows a similar trend prescribed by Eqs. (13) – (14). As r/H is small, the present study shows a τ trend similar to Phares *et al.* (2000) for S1 to S6. The radial location of the maximum wall shear stress is approximately the same as those predicted by Phares *et al.* (2000) impingement model, despite the presence of the arrays in the present study. However, due to a much higher Re in the present cases of microburst ($\text{Re} = 2.42 \times 10^9$), the wall shear stress is consistently much higher than those reported ($\text{Re} \sim O(10^4)$) by Phares et al. (2000). Except for S3, the τ of S1 to S6 are about two-orders higher than those reported by Phares et al. (2000). However, the reason is unknown for that of S3, which is three-order higher than those reported by Phares *et al.* (2000). A short distance after the maximum wall shear stress, there is a region of sudden large oscillation of the shear stress. This corresponds to the region of the urban array. Whenever the high speed microburst wind hits into the windward façade of a block within the array, the flow becomes stagnant at the facade. In this stagnation region, μ_{turb} becomes negligible, i.e. the flow is laminar. Hence at the windward façade of each block, a sudden drop in τ is observed. When the flow regains its turbulent kinetic energy on the roof, τ is observed to increase sharply, creating a sharp spiky peak close to the predicted value by the turbulent axisymmetric wall jet model of Poreh et al. (1967). Despite the oscillation in τ within the array, the sharp peak region is presented with a decaying behaviour over the spatial distribution along the

centreline of the array (i.e. the centreline of array is shown in Fig. 5). This feature is similar to the linear decaying behaviour predicted by Poreh et al. (1967) model.

3.3.1 Spatially-averaged wall shear stress along centreline of the array

The oscillatory portions of τ curves in Figs. 12(a) - (b) are due to the physical presence of the array at the corresponding locations. As aforementioned, the decaying behaviour of τ is similar to that of Poreh *et al.* (1967). Therefore, by using the methodology of Poreh et al. (1967) model and mean value theorem for single integrals (see Eq. (15)), Eq. (16) is proposed for estimating the spatially-averaged wall shear stress $\tau_{\text{average,1D}}$ along the centreline of the rectangular staggered array.

$$\tau_{\text{average,1D}} = \frac{1}{L_s} \int_D^{D+L_s} 0.34 \left(\frac{H}{D}\right)^{-2} \text{Re}^{-0.3} \rho U_{\text{jet}}^2 \left(\frac{r}{H}\right)^{-2.3} dx \quad (15)$$

$$\tau_{\text{average,1D}} = \frac{17}{65L_s} \rho^{0.7} U_{\text{jet}}^{1.7} \mu^{0.3} \left(\frac{H}{D}\right)^{0.3} \left[D^{0.7} - \frac{D^2}{(D + L_s)^{1.3}} \right] \quad (16)$$

where L_s is the length of the staggered arrays measured along the centreline of the arrays and μ is the dynamic viscosity of air.

To the authors' knowledge, there is no model currently that is capable of estimating the spatially-averaged wall shear stress of rectangular staggered arrays near the storm centre of a microburst using D , H and U_{jet} yet. The present model is, however, treated as independent of λ_F and λ_P .

To assess the difference in $\tau_{\text{average,1D}}$ obtained from CFD and Eq. (16), the percentage difference Δ is calculated by Eq. (17). The results of Δ for S1, S2, S3, S4, S5 and S6 are tabulated in Table 7.

$$\Delta = \left| \frac{(\tau_{\text{average,1D}} \text{ from CFD}) - (\tau_{\text{average,1D}} \text{ from Eq. (16)})}{(\tau_{\text{average,1D}} \text{ from Eq. (16)})} \times 100\% \right| \quad (17)$$

It is observed that the smallest combination of both λ_F and λ_P for a particular array yields the best estimation of $\tau_{\text{average,1D}}$ using Eq. (16), which is expected because Poreh *et al.* (1967) model was derived based on axisymmetric turbulent impinging jet without obstacles. The poorest estimation is S1 array (i.e. $\Delta = 57.9\%$) (Fig. 12a) since both the λ_F and λ_P are the largest ($\lambda_F = 0.347$ and $\lambda_P = 0.243$) among all the cases. The best estimation is S4 array (Fig. 12b) (i.e. $\Delta = 14.6\%$), since both the λ_F and λ_P ($\lambda_F = 0.084$ and $\lambda_P = 0.059$) are the lowest among all the cases. For S2, S3, S5 and S6 (not shown herein), their estimation accuracy is between that of S1 and S4 (ranging from $\Delta = 18\%$ to $\Delta = 27.6\%$) Hence, for large values of λ_F and λ_P , it is recommended to use CFD to determine $\tau_{\text{average,1D}}$.

A procedure for using Eq. (16) to estimate the spatially-averaged wall shear stress along the centreline of the staggered arrays for other values of H/D , D and U_{jet} equivalent to a full-scale microburst in nature is demonstrated with the aid of Fig. 13. Fig. 13 shows the variation of the estimated $\tau_{\text{average,1D}}$ within the range of possible H/D (i.e. $H/D = 0.75 - 7.5$) observed in full-scale microburst in nature (Zhang, 2013), while U_{jet} is fixed at the highest recorded speed of microburst in field measurements (i.e. $U_{\text{jet}} = 75\text{m/s}$ (Letchford *et al.*, 2002)) and $D = 500\text{m}$ is fixed at constant. The L_s is length of the array along the centreline used in the present study. Using this procedure, the $\tau_{\text{average,1D}}$ acting on an array-of-interest for other values of H/D are estimated, for a microburst with fixed downdraft diameter and speed, prior to CFD simulations. Likewise, the same procedure can be repeated to estimate the spatially-averaged wall shear stress along the centreline of the array for different values of U_{jet} and D that are associated with full-scale microburst in nature.

3.4 Effects of frontal and plan area density on surface pressure coefficient

In this section, the effects of λ_F and λ_P on mean surface pressure coefficient C_P around the block array is discussed. The C_P quantifies the pressure load of microburst flow acting on the arrays, and it is calculated as follows:

$$C_P = \frac{p - p_{\text{atm}}}{0.5\rho U_{\text{jet}}^2} \quad (18)$$

where p is the pressure, p_{atm} is the pressure of synoptic ambient wind. p_{atm} equal to zero in this study.

The published experimental data of C_p radial distribution versus X/D for the impinging jet flow without obstacles are included in Fig. 14 for comparison. The experimental data are obtained from Sengupta and Sarkar (2008) and Zhang *et al.* (2014b). It is observed that the results are Reynolds number independent for $Re > 27,000$ (Xu and Hangan, 2008); and there is no significant difference between our numerical results and those of the published experimental data for the region that is not within the array (i.e. $X/D < 0$ and $X/D > 4.68$). Hence, the flow field and wind load on the other side of the impinging jet $X/D < -1$ is not strongly affected by the array at $X/D < -1$. This implies that if there is another identical second array placed at the side without array at $X/D < -1$, the influence of the flow field and wind load on the array at $X/D < 1$ by the second array at $X/D < -1$ will be minimal. Therefore, the present results are also applicable to the case of two arrays that are oppositely-facing and equidistant from the impinging jet centre. Between $X/D = 0$ and $X/D = 4.68$, where the array is located, the sudden variation of C_p is found mainly between $X/D = 0$ and $X/D = 2.52$ approximately, which causes significant deviation from the experimental results of Sengupta and Sarkar (2008) and Zhang *et al.* (2014b). The first row of obstacles ($0 \leq x/D \leq 0.12$) has caused the magnitude of C_p to increase significantly. At $X/D = 0$, where the flow just encountered the windward wall of the first row of obstacles, the positive C_p is observed, similar to the isolated building configurations (Chay and Letchford, 2002; Zhang *et al.*, 2014b). At the leeward wall of the first row of obstacles, the value of C_p returns close to zero, and it is similar to the observed C_p at the leeward wall for isolated building configuration (Chay and Letchford, 2002). Within $0 \leq X/D \leq 2$, there is a larger variation of C_p . For $X/D > 2$, there is almost no significant difference between the present results and that of Sengupta and Sarkar (2008) and Zhang *et al.* (2014b).

Fig. 15 shows the span-wise variation of C_p versus Y/D at $X/D = 0$ (windward region). In Fig. 15, for all the array cases, the C_p along $X/D = 0$ is mildly negative around $y/D = 1$ and $y/D = -1$, which are due to the corners of the arrays. The C_p is observed to be higher within $y/D = -0.5$ and $y/D = 0.5$ than the rest of the regions. Between $y/D = 1$ and $y/D = -1$, there are oscillation of C_p with large amplitude. The C_p minima could be due to the presence of un-blocked regions. The time-mean velocity of S6 at the level $0.5H$ above the

ground in Fig. 16 is used to show an un-blocked region (marked ‘C’) that corresponds to the C_p minima of S6 (marked ‘C’) in Fig. 15. The C_p maxima of S6 (marked ‘O’ in Fig. 15) is associated with a blocked region (marked ‘O’ in Fig. 16). By considering the velocity field around S6 in Fig. 16 together with the variation of C_p distribution in Fig. 15, the C_p maxima and minima in the pressure fields, correspond to the flow with high momentum impinging on the obstacles and the channelled flow (inter-obstacle spacing) regions. The deceleration of the flow with high momentum at the blocked regions eventually causes pressure build-up, and therefore, the C_p is distinctly higher than those at the inter-obstacle spacing.

Fig. 17 shows the span-wise variation of C_p versus Y/D at $X/D = 4.68$ (leeward region). For all the array cases, the C_p distribution for all the array cases appears to be asymmetrical about $Y/D = 0$. Using the contour plot of the mean velocity at the level $0.5H$ above the ground for S6 as an example (see Fig. 16), the asymmetry of C_p is due to the staggered arrangement of the obstacles blocking the flow. Certain locations contain the negative C_p , which can be regarded as regions of suction (Li and Ou, 2012). At $Y/D = 1$ along the $X/D = 4.68$ (marked ‘K’ on Fig. 16), the flow is not directly sheltered by an obstacle, thus resulting in higher C_p than those observed at $Y/D = -1$ along $X/D = 4.68$ (marked ‘T’ on Fig. 16). As the velocity field in Fig. 16 suggests, the higher C_p is a result of the higher momentum that the fluid carries at point K than those at point T. In addition, the longer wake distance between point K and the obstacle in front of it also could have aided the flow in regaining more pressure; it results in higher C_p at point K than those at point T.

Fig. 18 shows the vertical variation of C_p versus Z/D on the centreline at (a) $X/D = 0$ (windward region) and (b) $X/D = 4.68$ (leeward region). Although some variations can be observed, there is no consistent relationship between various values of λ_F or λ_P and vertical variation of C_p in the present study. The windward C_p (see Fig. 18(a)), excluding S4 and S5, shows larger variation than those in the leeward region (see Fig. 18(b)) near the ground. This might be because being close to the downdraft region which is $r/D = 1$ away, the reported maximum velocity near the ground (Kim and Hangan, 2007) transferred a large amount of momentum from the flow to the obstacle (due to the deceleration of flow), causing the C_p to be relatively much larger than those around the mid-height segment ($Z/D = 0.05$). Beyond $1.1D$ from the downdraft centre, Kim and Hangan (2007) reported that the velocity near ground decays with radial distance from the stagnation flow region. Therefore, the

momentum transferred by the fluid in the leeward region near the ground is relatively smaller, and this causes C_p to be smaller. For S4 and S5, the lack of large variation in C_p close to the ground, may be due to the smaller λ_p . (i.e. $\lambda_p = 0.059$ for S4 and $\lambda_p = 0.108$ for S5).

3.5 Pressure drag and viscous drag force

The total streamwise drag force D_{total} is the sum of pressure drag D_p and viscous drag D_v forces. According to the open literature, in the study of ABL flow over surface roughness, one of the methodologies used to estimate the D_{total} is by integrating front-to-back pressure difference distribution obtained from pressure taps across obstacles in wind tunnel. The underlying assumption for the pressure-tapped measurement has to be an insignificant amount of D_v relative to the D_{total} . The fact that D_v is negligible relative to the D_{total} implies that the flow is weakly dependent on Reynolds number (Castro, 2007). Some examples of experimental studies who have employed this technique for ABL flow over arrays with various roughness are: Cheng and Castro (2002) and Cheng *et al.* (2007). In more recent years, this technique has been employed in the study of microburst-induced drag force acting on high-rise building, which is published by Zhang *et al.* (2014b). For ABL flow normal to the windward façade of the obstacles (i.e. 0° inflow angle), Cheng *et al.* (2007) showed that the ratio of D_p to D_{total} acting on a cubic staggered array is between 1.03 and 1.12 for $\lambda_p = \lambda_F = 0.0625$ and $\lambda_p = \lambda_F = 0.25$ at Reynolds number $Re_T = 1.2 \times 10^4$ (based on the inlet mean velocity and an obstacle height). They commented that the magnitude of D_p is larger than D because of error in measurement techniques. Leonardi and Castro (2010) studied the D_v acting on staggered cubic array (i.e. $\lambda_p = \lambda_F = 0.04 - 0.25$) for a ABL wind at 0° inflow angle using DNS at $Re_T = 7,000$. They showed that the ratio of D_v to D_p is about 0.18 when $\lambda_p = 0.04$ and 0.077 when $\lambda_p = 0.25$. Zaki *et al.* (2012) studied the neutrally stratified ABL flow ($Re_T \approx 2 \times 10^4$) over cubical staggered arrays with $\lambda_p = \lambda_F = 0.077, 0.174, 0.309$ at 0° oncoming wind direction in a wind tunnel. Zaki *et al.* (2012) reported that the ratio of D_p to D_{total} was estimated to be close to unity (less than 5% difference from unity). To the authors' knowledge, none of the work in the open literature has

investigated whether D_v can be regarded as insignificant relative to the D_p for the microburst wind flowing past the staggered array configurations. In this section, the contributions of the D_p and D_v to the D for S1, S2, S3, S4, S5 and S6 at 0° oncoming microburst wind direction will be presented.

Fig. 19 shows the D_v/D_p ratio versus the λ_p obtained from the present study together with those of neutrally stratified ABL wind flowing past staggered arrays, published in the experimental study ($Re_T = 7,000$) by Leonardi and Castro (2010) and the DNS study ($Re_T \approx 2 \times 10^4$) by Zaki *et al.* (2012). It is observed that there is a great difference in D_v/D_p between those of neutrally stratified ABL and microburst in general. Apart from the type of wind, the difference in the D_v/D_p between ABL and microburst wind could possibly be due to Reynolds number effect since the increase in Re_T for the ABL wind can also causes the reduction in D_v/D_p observed especially at the smaller range of λ_p . Leonardi and Castro (2010) also commented that if λ_p of a staggered array is as small as 0.04 in their study, the obstacles in staggered arrays can be treated as individual obstacles. Hence, this might be the reason why the D_v/D_p results for S4 (i.e. $\lambda_p = 0.059$) is very much in agreement with those of Zhang *et al.* (2014b)'s experimental study on isolated high-rise building model.

Overall, the viscous drag force relative to the total drag force, within the investigated range of packing densities, is insignificant to the total drag force. Therefore, the viscous drag force can be neglected. The present finding will be able to provide a preliminary assessment of the error uncertainty associated with the 'pressure-tap' experimental technique used in the determination the total drag force magnitude exerted on staggered arrays by microburst-like wind in laboratory.

3.6 Ratio of mean vertical lift force to resultant force in the vertical plane

According to the open literature, there are very few investigations of the mean vertical lift force exerted by microburst wind on surface-mounted obstacles. None of the studies in the open literature has investigated the effect of packing density of staggered arrays on the mean total vertical lift force (L) acting on such array. In this section, the effects of roughness packing densities (λ_p and λ_F) of staggered array on the L , in terms of the ratio of L to the steady resultant force magnitude T (i.e. L/T) in the vertical X-Z plane, are discussed. The

ratio of total drag to the resultant force magnitude D_{total}/T is also investigated. The L/T and D_{total}/T ratios are equivalent to the ratios of $L/N : T/N$ and $D_{\text{total}}/N : T/N$ respectively, where N is the total number of blocks in an array. L/N is the averaged lift force per block, D_{total}/N is the averaged drag force per block, T/N is the averaged resultant force per block in the X-Z plane. The value of T can be computed by:

$$T = \sqrt{D_{\text{total}}^2 + L^2} \quad (19)$$

Fig. 20 shows the effect of λ_F on the L/T and D_{total}/T ratios. The L/T ratio is also found to be consistently lower than the D_{total}/T ratio for $0.118 \leq \lambda_F \leq 0.347$ while λ_P is fixed at 0.243. As λ_F increases, the ratio L/T decreases. In contrast, the D_{total}/T ratio increases as λ_F increases. According to the aforementioned section on C_D (section 3.2), the λ_F can be used to characterise the mutual sheltering effect in arrays (Shao and Yang, 2005). For the mutual sheltering effect to dominate an effective force term, it is observed in section 3.2 that the mutual interference among the obstacles becomes greater as λ_F increases, thus resulting in a decrease in the capacity of the surface to absorb momentum as λ_F increases. Hence, in the present study, the mutual sheltering effect is observed to dominate L/T for $0.118 \leq \lambda_F \leq 0.347$ while λ_P is fixed at 0.243.

Fig. 21 shows the effect of λ_P on the L/T and D_{total}/T ratios. The L/T ratio is found to be consistently lower than the D_{total}/T ratio for $0.059 \leq \lambda_P \leq 0.181$ values while λ_F is fixed at 0.084. As λ_P increases, the L/T ratio increases. In contrast, the D_{total}/T ratio decreases as λ_P increases. It means that the mutual sheltering effect does not dominate the L/T ratio for $0.059 \leq \lambda_P \leq 0.181$ values while λ_F is fixed at 0.084 in the present study.

For S4, which has the smallest λ_F and λ_P values among the other arrays (i.e. $\lambda_P = 0.059$ and $\lambda_F = 0.084$), the L/T ratio is about 0.30, which is the smallest L/T among the other arrays. In addition, the smallest L/D_{total} ratio is also found in S4 ($L/D_{\text{total}} = 0.32$), shown in Fig. 22. Based on published literatures, the λ_F and λ_P values of S4 in the present study is in the lower range of packing densities. For instance, the lower extreme range of the λ_P (and λ_F is equal to λ_P since cubical obstacle were used) in the work of Leonardi and Castro (2010) was 0.04, which the obstacles in the array can be regarded as individual elements. Cheng *et*

al. (2007) studied the staggered arrays of different packing density. The smallest packing density was $\lambda_p = \lambda_F = 0.0625$. Thus, the vertical lift ratios for S4 (i.e. $L/T=0.30$ and $L/D_{total}=0.32$) can also be regarded as an approximation of the averaged vertical lift force acting on individual obstacles.

Based on the L/T and L/D_{total} ratios in the present study, the lift force relative to the resultant and drag force acting on per building cannot be neglected because L is about 0.3 to 0.6-0.7 times of T and D_{total} (see Figs. 21 to 22) for packing densities within $0.118 \leq \lambda_F \leq 0.347$ and $0.059 \leq \lambda_p \leq 0.181$, despite that there might be some mutual sheltering effect between obstacles to reduce the force ratios. Therefore, the vertical force has to be taken into account during the design and maintenance of high-rise buildings, particularly the high-rise buildings built in cities within the packing densities of $0.118 \leq \lambda_F \leq 0.347$ and $0.059 \leq \lambda_p \leq 0.181$.

4. Conclusion

In this paper, the microburst aerodynamic quantities and wind load effect in urban environment are studied using RANS together with the $k - \omega$ SST turbulence model. Blocks and rectangular arrays are simplified models of high-rise buildings and urban environment. The drag force, wall shear stress in the array area, the pressure distribution as well as the mean vertical lift force have been computed to investigate the effects of wind load exerted on the array configurations. Their variations are studied by considering the effects of λ_F , and λ_p . The main results are summarised as follows.

1. The $k - \omega$ SST turbulence model, together with the standard wall function, is found capable of modelling for steady impinging jets with the application of microburst simulations.
2. For $0.118 \leq \lambda_F \leq 0.347$ and $\lambda_p = 0.243$, C_D decreases as λ_F increases. The decrease of C_D is possibly due to mutual sheltering effect that dominates the microburst flow in the staggered array herein.
3. For $0.059 \leq \lambda_p \leq 0.181$ and $\lambda_F = 0.084$, C_D increases as λ_p increases,. The trend is similar to those of ABL wind. Furthermore, the mutual sheltering effect does not dominate the microburst flow in the staggered array herein.

4. The effect of λ_F and λ_P on τ distribution within the array cause the wall shear stress to have large, sudden fluctuations. Nonetheless, the general trend is in good agreement with the predicted wall shear stress by Poreh *et al.* (1967) model for a turbulent axisymmetric radial impinging jet on smooth surface.
5. Based on Poreh *et al.* (1967) model, an expression is proposed to estimate the microburst's spatially-averaged wall shear stress along the centreline of the staggered arrays. The estimation is about 14.6% - 27.6% deviating from the computed results for the investigated staggered array, i.e. S2, S3, S4, S5 and S6. However, CFD is still recommended to determine the spatially-averaged wall shear stress for values of λ_F and λ_P larger than those of S2, S3, S4, S5 and S6.
6. In the windward region of the array, if the microburst flow is blocked by an obstacle, C_P in front of the first row of obstacles in the array will generally be higher than those of channelled flow region. In the leeward side, C_P is generally lower if the location is blocked directly by the last row of obstacles of the arrays.
7. The C_P distributions outside of the arrays S1, S2, S3, S4, S5 and S6 have shown good agreement with those of published experiment without any array in general.
8. The viscous drag force relative to the total drag force for various packing densities is insignificant to the total drag force, and therefore it can be neglected. This finding will provide a preliminary assessment of the error uncertainty present in the 'pressure-tap' experimental method for determining the total drag exerted on staggered arrays by microburst-like wind in laboratory.
9. The vertical lift force relative to the resultant force acting on per building cannot be neglected. The mean vertical lift force should be taken into account during the design and the maintenance routines of high-rise buildings, particularly for the high-rise buildings built in cities for packing densities within $0.118 \leq \lambda_F \leq 0.347$ and $0.059 \leq \lambda_P \leq 0.181$.

The present study should be taken as tentative, and comparisons with models. Full-scale measurements are required before a conclusion regarding the validity of the present results can be given. However, in the meantime, the present results should be useful for engineering purposes in making assessment in relation to the wind load effects of microbursts.

Acknowledgement

The authors would like to thank Energy Research Institute (ERI@N) under Nanyang Technological University (NTU, Singapore) and Norwegian Marine Technology Research Institute (MARINTEK, Norway) for their support during this project. The first author would also like to thank the National Research Foundation (NRF, Singapore) for funding his Ph.D. studies. The second author would like to thank NOWITECH (Norwegian Research Centre for Offshore Wind Technology), which is co-funded by the Research Council of Norway, industrial companies and participating research organizations, for the support.

References

- ASCE7-05, 2005. ASCE standard, minimum design loads for buildings and other structures, America Society of Civil Engineers (ASCE), New York, USA.
- Blocken, B., Stathopoulos, T., Carmeliet, J., 2007. CFD simulation of the atmospheric boundary layer: wall function problems. *Atmospheric Environment* 41, 238-252.
- Castro, I.P., 2007. Rough-wall boundary layers: mean flow universality. *Journal of Fluid Mechanics* 585, 469-485.
- Chay, M.T., Letchford, C.W., 2002. Pressure distributions on a cube in a simulated thunderstorm downburst—Part A: stationary downburst observations. *Journal of Wind Engineering and Industrial Aerodynamics* 90, 711-732.
- Cheng, H., Castro, I., 2002. Near Wall Flow over Urban-like Roughness. *Boundary-Layer Meteorol* 104, 229-259.
- Cheng, H., Hayden, P., Robins, A.G., Castro, I.P., 2007. Flow over cube arrays of different packing densities. *Journal of Wind Engineering and Industrial Aerodynamics* 95, 715-740.
- Choi, E.C.C., 2004. Field measurement and experimental study of wind speed profile during thunderstorms. *Journal of Wind Engineering and Industrial Aerodynamics* 92, 275-290.
- Coceal, O., Thomas, T.G., Castro, I.P., Belcher, S.E., 2006. Mean Flow and Turbulence Statistics Over Groups of Urban-like Cubical Obstacles. *Boundary-Layer Meteorol* 121, 491-519.
- Cooper, D., Jackson, D.C., Launder, B.E., Liao, G.X., 1993. Impinging jet studies for turbulence model assessment—I. Flow-field experiments. *International Journal of Heat and Mass Transfer* 36, 2675-2684.
- Ferziger, J.H., Peric, M., 2001. *Computational Methods for Fluid Dynamics*, 3rd ed. Springer-Verlag, Berlin, Germany.

Franke, J., Hirsch, C., Jensen, A., Krüs, H., Schatzmann, M., Westbury, P., Miles, S., Wisse, J., Wright, N., 2004. Recommendations on the use of CFD in wind engineering, Cost Action C, p. C1.

Fujita, T.T., 1981. Tornadoes and Downbursts in the Context of Generalized Planetary Scales. *Journal of the Atmospheric Sciences* 38, 1511-1534.

Fujita, T.T., 1985. The downburst: microburst and macroburst : report of projects NIMROD and JAWS. Satellite and Mesometeorology Research Project, Dept. of the Geophysical Sciences, University of Chicago, United States.

Grimmond, C.S.B., Oke, T.R., 1999. Aerodynamic Properties of Urban Areas Derived from Analysis of Surface Form. *Journal of Applied Meteorology* 38, 1262-1292.

Hangan, H., Xu, Z., 2005. Scale, roughness and initial conditions effects in impinging jets with application to downburst simulations, In: Proceedings of the 10th Americas Conference on Wind Engineering (10ACWE), Baton Rouge, LA, USA.

Hjelmfelt, M.R., 1988. Structure and Life Cycle of Microburst Outflows Observed in Colorado. *Journal of Applied Meteorology* 27, 900-927.

Kim, J., Hangan, H., 2007. Numerical simulations of impinging jets with application to downbursts. *Journal of Wind Engineering and Industrial Aerodynamics* 95, 279-298.

Kim, J., Hangan, H., Ho, T.C.E., 2007. Downburst versus boundary layer induced wind loads for tall buildings. *Wind and Structures* 10, 481-494.

Leonardi, S., Castro, I.P., 2010. Channel flow over large cube roughness: a direct numerical simulation study. *Journal of Fluid Mechanics* 651, 519-539.

Letchford, C.W., Mans, C., Chay, M.T., 2002. Thunderstorms—their importance in wind engineering (a case for the next generation wind tunnel). *Journal of Wind Engineering and Industrial Aerodynamics* 90, 1415-1433.

Li, C., Li, Q.S., Xiao, Y.Q., Ou, J.P., 2012. A revised empirical model and CFD simulations for 3D axisymmetric steady-state flows of downbursts and impinging jets. *Journal of Wind Engineering and Industrial Aerodynamics* 102, 48-60.

Li, H., Ou, J., 2012. Experimental simulation of downburst-generated wind loading on building structure, The Seventh International Colloquium on Bluff Body Aerodynamics and Application (BBAA7), Shanghai, China.

Mårtensson, G., Skote, M., Malmqvist, M., Falk, M., Asp, A., Svanvik, N., Johansson A.V., 2006. Rapid PCR amplification of DNA utilizing Coriolis effects. *European Biophysics Journal* 35, 453-458.

Mason, M.S., Letchford, C.W., James, D.L., 2005. Pulsed wall jet simulation of a stationary thunderstorm downburst, Part A: Physical structure and flow field characterization. *Journal of Wind Engineering and Industrial Aerodynamics* 93, 557-580.

- Mason, M.S., Wood, G.S., Fletcher, D.F., 2009. Numerical simulation of downburst winds. *Journal of Wind Engineering and Industrial Aerodynamics* 97, 523-539.
- Menter, F.R., 1994. Two-equation eddy-viscosity turbulence models for engineering application." *AIAA J.* 32, 1598-1605.
- Nicholls, M., Pielke, R., Meroney, R., 1993. Large eddy simulation of microburst winds flowing around a building. *Journal of Wind Engineering and Industrial Aerodynamics* 46 & 47, 229-237.
- Ong, M.C., Utnes, T., Holmedal, L.E., Myrhaug, D., Pettersen, B., 2009. Numerical simulation of flow around a smooth circular cylinder at very high Reynolds numbers. *Marine Structures* 22, 142-153.
- OpenFOAM, 2014. available at: <http://www.openfoam.org/docs/user/>.
- Oseguera, R.M., Bowles, R.L., 1988. A Simple, Analytic 3-dimensional Downburst Model Based on Boundary Layer Stagnation Flow.
- Padhra, A., 2010. Estimating the sensitivity of urban surface drag to building morphology, Department of Meteorology. University of Reading, UK.
- Phares, D.J., Smedley, G.T., Flagon, R.C., 2000. The wall shear stress produced by the normal impingement of a jet on a flat surface. *Journal of Fluid Mechanics* 418, 351-375.
- Poreh, M., Tsuei, Y.G., Cermak, J.E., 1967. Investigation of a Turbulent Radial Wall Jet. *Journal of Applied Mechanics* 34, 457-463.
- Schatzmann, M., Olesen, H.R., Franke, J., 2010. COST 732 model evaluation case studies: approach and results. COST Office, Hamburg, Germany.
- Sengupta, A., Sarkar, P.P., 2008. Experimental measurement and numerical simulation of an impinging jet with application to thunderstorm microburst winds. *Journal of Wind Engineering and Industrial Aerodynamics* 96, 345-365.
- Shao, Y., Yang, Y., 2005. A scheme for drag partition over rough surfaces. *Atmospheric Environment* 39, 7351-7361.
- Skote, M., Sandberg, M., Westerberg, U., Claesson, L., Johansson, A.V., 2005. Numerical and experimental studies of wind environment in an urban morphology. *Atmospheric Environment* 39, 6147-6158.
- Skote, M., 2014. Scaling of the velocity profile in strongly drag reduced turbulent flows over an oscillating wall. *International Journal of Heat and Fluid Flow* 50, 352—358.
- Sweby, P.K., 1984. High resolution schemes using flux limiters for hyperbolic conservation laws. *SIAM journal on numerical analysis* 21, 995-1011.

Theurer, W., Baechlin, W., Plate, E.J., 1992. Model study of the development of boundary layers above urban areas. *Journal of Wind Engineering and Industrial Aerodynamics* 41, 437-448.

Tian, X., Ong, M.C., Yang, J., Myrhaug, D., 2013. Unsteady RANS simulations of flow around rectangular cylinders with different aspect ratios. *Ocean Engineering* 58, 208-216.

United States Federal Aviation Administration. (1988). Pilot windshear guide. United States

Versteeg, H.K., Malalasekera, W., 2007. *An Introduction to Computational Fluid Dynamics: The Finite Volume Method*. Pearson Education Limited, England, United Kingdom.

Vicroy, D.D., 1991. A simple, analytical, axisymmetric microburst model for downdraft estimation [microform] / Dan D. Vicroy, in: United States. Federal Aviation, A., Langley Research, C. (Eds.), NASA technical memorandum ; 104053. National Aeronautics and Space Administration, Langley Research Center, Hampton, Va.

Viskanta, R., 1993. Heat transfer to impinging isothermal gas and flame jets. *Experimental Thermal and Fluid Science* 6, 111-134.

Wood, G.S., Kwok, K.C.S., Motteram, N.A., Fletcher, D.F., 2001. Physical and numerical modelling of thunderstorm downbursts. *Journal of Wind Engineering and Industrial Aerodynamics* 89, 535-552.

Xu, Z., Hangan, H., 2008. Scale, boundary and inlet condition effects on impinging jets. *Journal of Wind Engineering and Industrial Aerodynamics* 96, 2383-2402.

Zaki, S.A., Hagishima, A., Tanimoto, J., 2012. Experimental study of wind-induced ventilation in urban building of cube arrays with various layouts. *Journal of Wind Engineering and Industrial Aerodynamics* 103, 31-40.

Zhang, Y., 2013. Study of microburst-like wind and its loading effects on structures using impinging jet and cooling source approach. PhD thesis. Iowa State University, p. 242, United States.

Zhang, Y., Hu, H., Sarkar, P.P., 2014a. Comparison of microburst-wind loads on low-rise structures of various geometric shapes. *Journal of Wind Engineering and Industrial Aerodynamics* 133, 181-190.

Zhang, Y., Sarkar, P., Hu, H., 2013. An experimental study of flow fields and wind loads on gable-roof building models in microburst-like wind. *Experiments in Fluids* 54, 1-21.

Zhang, Y., Sarkar, P., Hu, H., 2014b. An experimental study on wind loads acting on a high-rise building model induced by microburst-like winds. *Journal of Fluids and Structures* 50, 547-564.

Zuckerman, N., Lior, N., 2005. Impingement heat transfer: correlations and numerical modeling. *Transactions of the ASME-C-Journal of Heat Transfer* 127, 544.

Figure Captions

- Fig. 1 Schematic cross-section through a symmetric microburst (Reproduced from United States Federal Aviation Administration (1998))
- Fig. 2 Full three-dimensional computational domain without array from (a) top and (b) front perspectives
- Fig. 3 Example of a staggered array using configuration S1
- Fig. 4 Relevant morphology dimensions for calculating λ_P and λ_F (Reproduced from Grimmond and Oke, 1999)
- Fig. 5 Full three-dimensional computational domain with array from front perspectives. (Z-coordinates are not shown in this figure)
- Fig. 6 Mesh of the case without array
- Fig. 7 Mesh for case with array S5: (a) around the upstream first two row, (b) around two intermediate rows of buildings
- Fig. 8 (Color online). Time-averaged vertical profile of radial velocity from field measurements, experiments, numerical simulations and semi-empirical models at $r/D=1$
- Fig. 9 Time-averaged vertical profile of radial velocity for impinging jet. (a) $r/D = 1$, (b) $r/D = 1.4$, (c) $r/D=2.0$, and (d) $r/D = 2.5$.
- Fig. 10 Variation of time-averaged C_D with λ_F (for S1, S2 and S3)
- Fig. 11 Variation of time-averaged C_D with λ_P (for S4, S5, S6)
- Fig. 12 Time-averaged wall shear stress along the x-axis for cases: (a) S1, (b) S4. Present results at $Re = 2.41 \times 10^9$ and Poreh *et al.* (1967 wall jet model at $Re = 2.41 \times 10^9$; Phares *et al.* (2000). impingement zone model at $Re \sim O(10^4)$ and $H/D = 2$.
- Fig. 13 Variation of spatially-averaged wall shear stress with H/D ratio along the centreline of array array (U_{jet} is kept constant at 75m/s, the highest recorded speed from field measurement, D is 500m and L_s is kept to the length of the

array used in the present study)

- Fig. 14 Comparison of C_p along the X-axis for S1, S2, S3, S4, S5 and S6. Sengupta and Sarkar (2008), and Zhang *et. al.* (2014b) experimental results (without obstacles) are included.
- Fig. 15 (Color online). Variation of C_p along span-wise direction at $x/D = 0$
- Fig. 16 The mean velocity contour plot of S6 at the level $0.5H$ above the ground
- Fig. 17 (Color online). Variation of C_p along span-wise direction at $x/D = 4.68$
- Fig. 18 Variation of C_p in vertical direction at (a) $x/D = 0$, (b) $x/D = 4.68$ on the centreline of array
- Fig. 19 D_v/D_p from the present simulation versus λ_p . Also included are: ABL flow over staggered cube array from Zaki *et. al.* (2012)'s experimental study ($Re_T \approx 2 \times 10^4$) and Leonardi and Castro (2010)'s DNS study ($Re_T = 7,000$)
- Fig. 20 Variation of L/T and D/T for various λ_F
- Fig. 21 Variation of L/T and D/T for various λ_p
- Fig. 22 Variation of L/D for various arrays

Table 1 Simulated cases

Cases	Contains array?	D (m)	H/D	Re
A1	No	0.0381	2, 4	2×10^4
S1	Yes	500	2	2.42×10^9
S2				
S3				
S4				
S5				
S6				

Table 2 Boundary conditions of computational domain for A1

Inlet (Dirichlet)	$(u_1, u_2, u_3) = (0, 0, -7.56)\text{m/s}$
	Turbulence intensity = 1%
	Reference length = 38.1mm
	$p = \text{zero normal gradient}$
Ground (wall)	No-slip condition $(u_1, u_2, u_3) = (0, 0, 0) \text{ m/s}$
	$p = \text{zero normal gradient}$
	Standard wall functions for velocity and turbulence
Pressure outlet	Turbulence intensity = 1%
	Reference length = 38.1mm
	$p = 0 \text{ Pa}$
Cylinder (Slip wall)	Slip conditions for (u_1, u_2, u_3) , p , k and ω .

Table 3 Dimensions of obstacles and inter-obstacle spacing

No.	Height of arrays	Number of obstacles in arrays	Plan Area Index, λ_P	Frontal Area Index, λ_F
S1	50m	406	0.243	0.347
S2		105		0.176
S3		50		0.118
S4		105	0.059	0.084
S5		45	0.108	
S6		36	0.181	

Table 4 Boundary conditions of computational domain for S1, S2, S3, S4, S5 and S6.

Inlet (Dirichlet)	$(u_1, u_2, u_3) = (0, 0, -75)\text{m/s}$
	Turbulence intensity = 1%
	Reference length = 500m
	$p = \text{zero normal gradient}$
Ground (wall)	No-slip condition $(u_1, u_2, u_3) = (0, 0, 0) \text{ m/s}$
	$p = \text{zero normal gradient}$
	Standard smooth wall functions for velocity and turbulence.
Pressure outlet	Turbulence intensity = 1%
	Reference length = 500m
	$p = 0 \text{ Pa}$
Cylinder (Slip wall)	Slip conditions for (u_1, u_2, u_3) , p , k and ω .
Array (wall)	No-slip condition
	$p = \text{zero normal gradient}$
	Standard smooth wall functions for velocity and turbulence.

Table 5 Results of A1 with different grid resolutions

Mesh case	Elements	$ U_{\text{peak}} /U_{\text{jet}}$	Percentage difference in $ U_{\text{peak}} /U_{\text{jet}}$ relative to mesh 1 (%)
1	1,825,320	0.960	-
2	2,740,744	0.961	0.104
3	4,110,021	0.960	0.000

Table 6 Results of S1, S2, S3, S4, S5 and S6 with different grid resolutions

Arrays	Mesh labels	Elements	C_D	Percentage difference in C_D relative to mesh 1 (%)
S1	1	11,703,514	0.602	
	2	17,605,183	0.599	-0.498
S2	1	12,930,988	0.651	
	2	19,396,361	0.651	0.000
S3	1	13,872,103	0.686	
	2	21,104,290	0.684	-0.292
S4	1	10,777,498	0.540	
	2	16,503,838	0.535	-0.926
S5	1	10,621,070	0.570	
	2	16,265,329	0.571	0.175
S6	1	11,200,200	0.672	
	2	16,923,892	0.673	0.149

Table 7 Percentage difference Δ of $\tau_{\text{average,1D}}$ computed by CFD, relative to Eq. (16).

Array cases	Δ
S1	57.9%
S2	27.6%
S3	18.0%
S4	14.6%
S5	26.4%
S6	21.7%

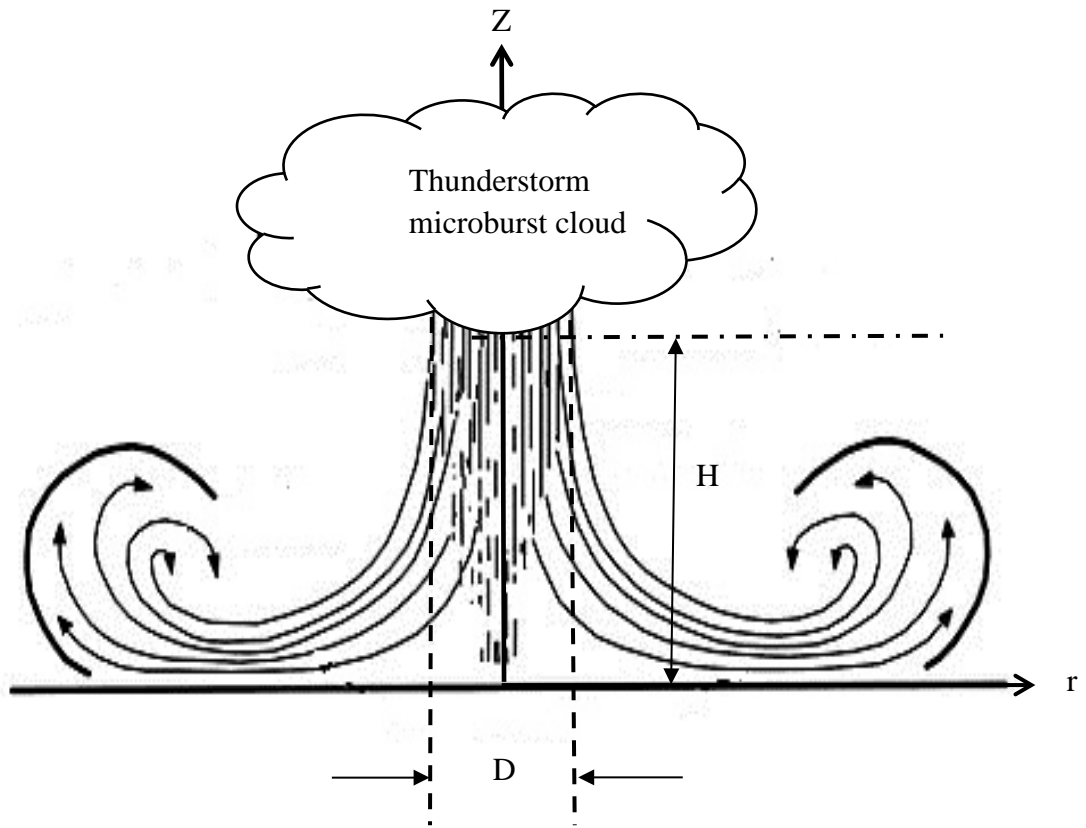
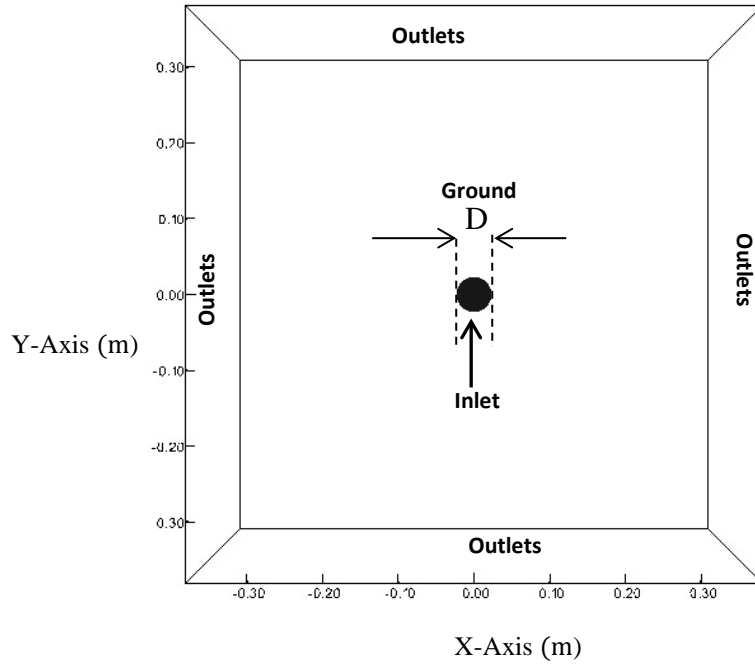


Fig. 1 Schematic cross-section through a symmetric microburst (Reproduced from United States Federal Aviation Administration (1988))

a



b

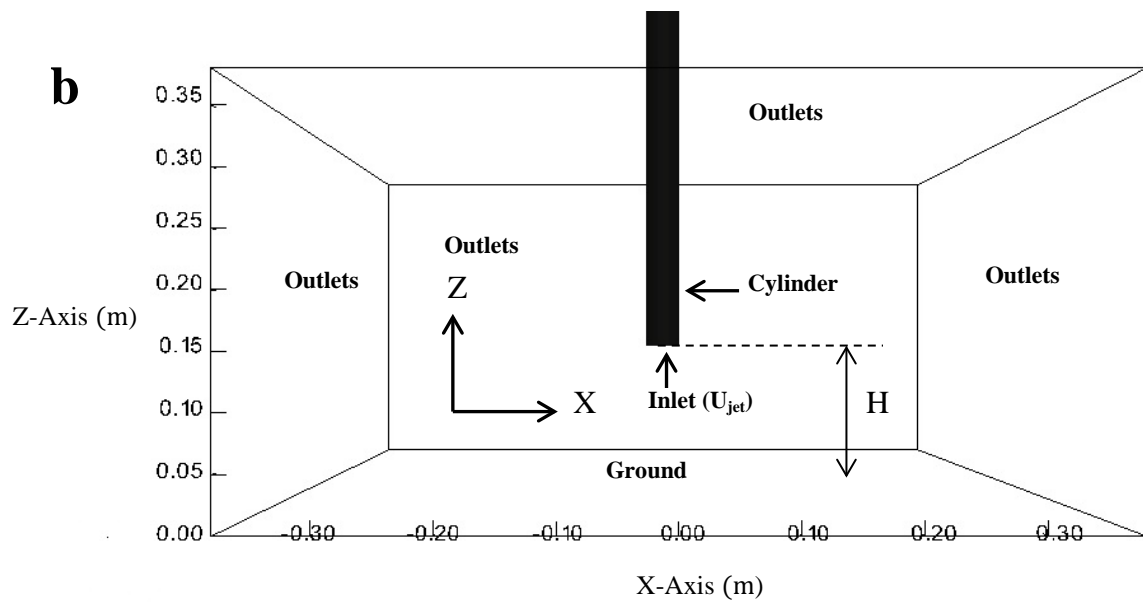


Fig. 2 Full three-dimensional computational domain without array from (a) top and (b) front perspectives

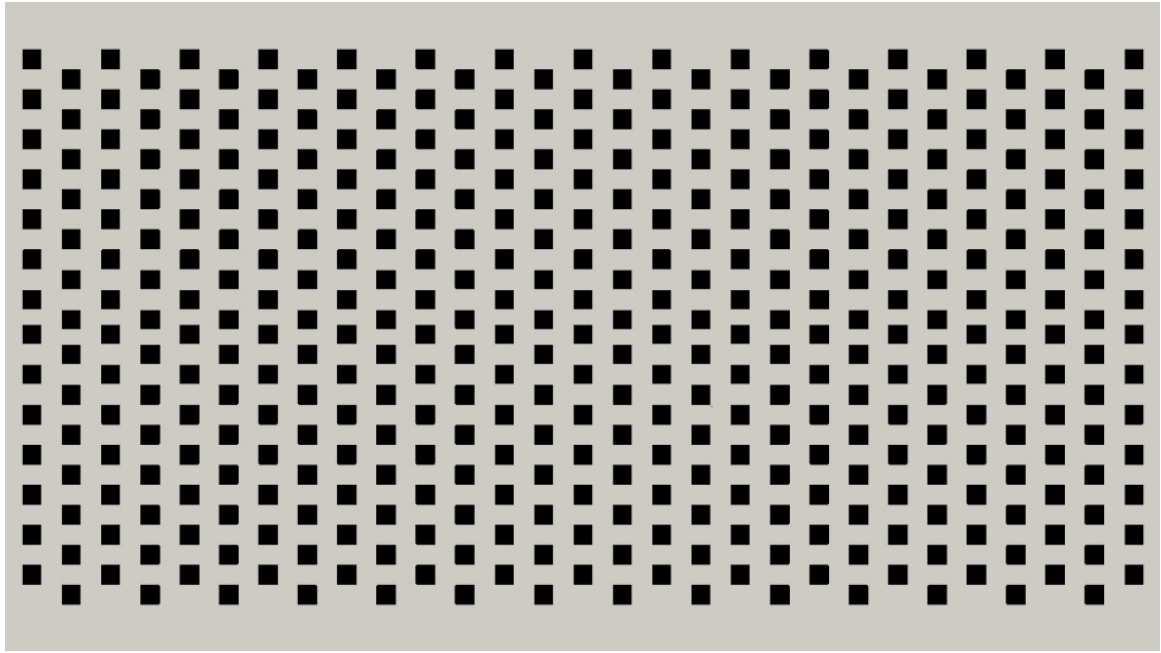


Fig. 3 Example of a staggered array using configuration S1

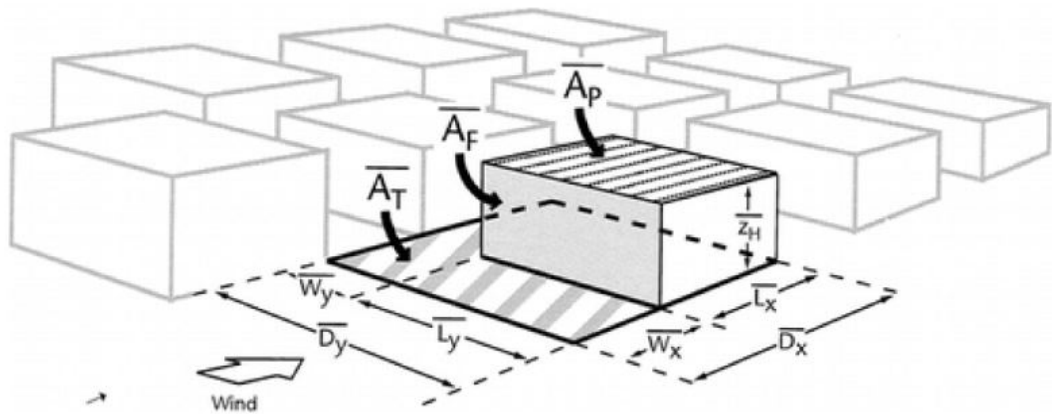


Fig. 4 Relevant morphology dimensions for calculating λ_p and λ_F (Reproduced from Grimmond and Oke, 1999)

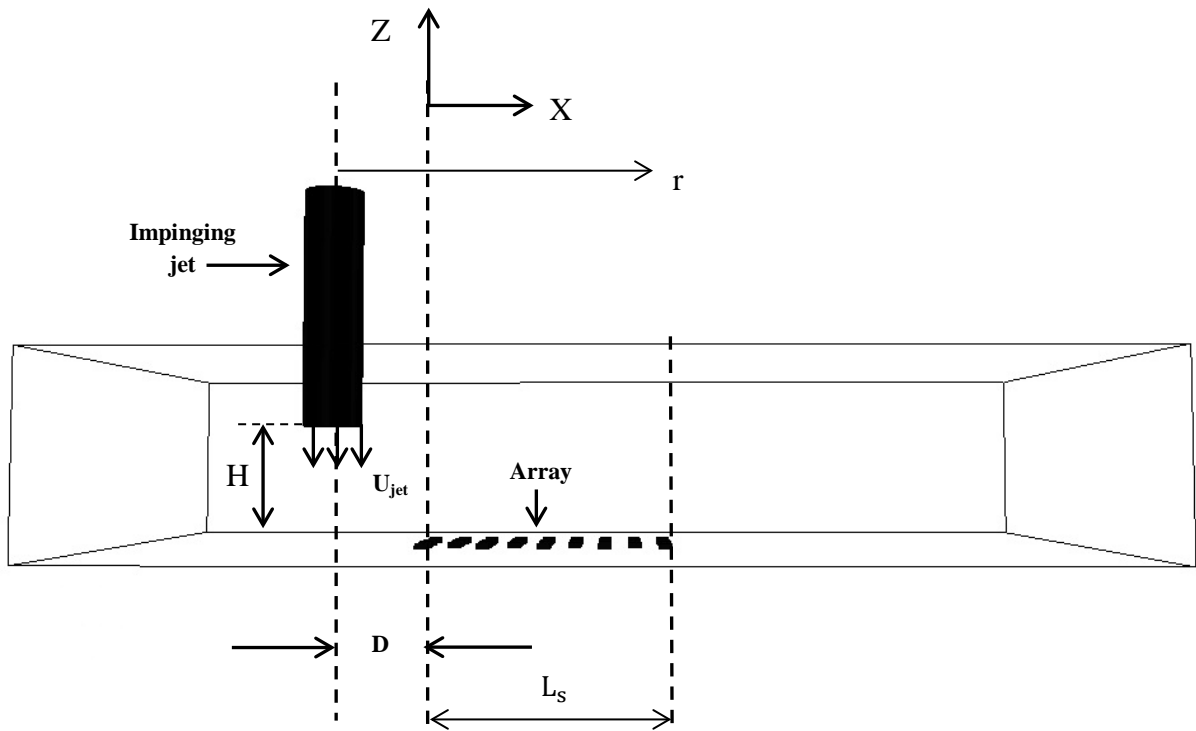


Fig. 5 Full three-dimensional computational domain with array S6 from front perspectives (Z-coordinates is not shown in this figure)

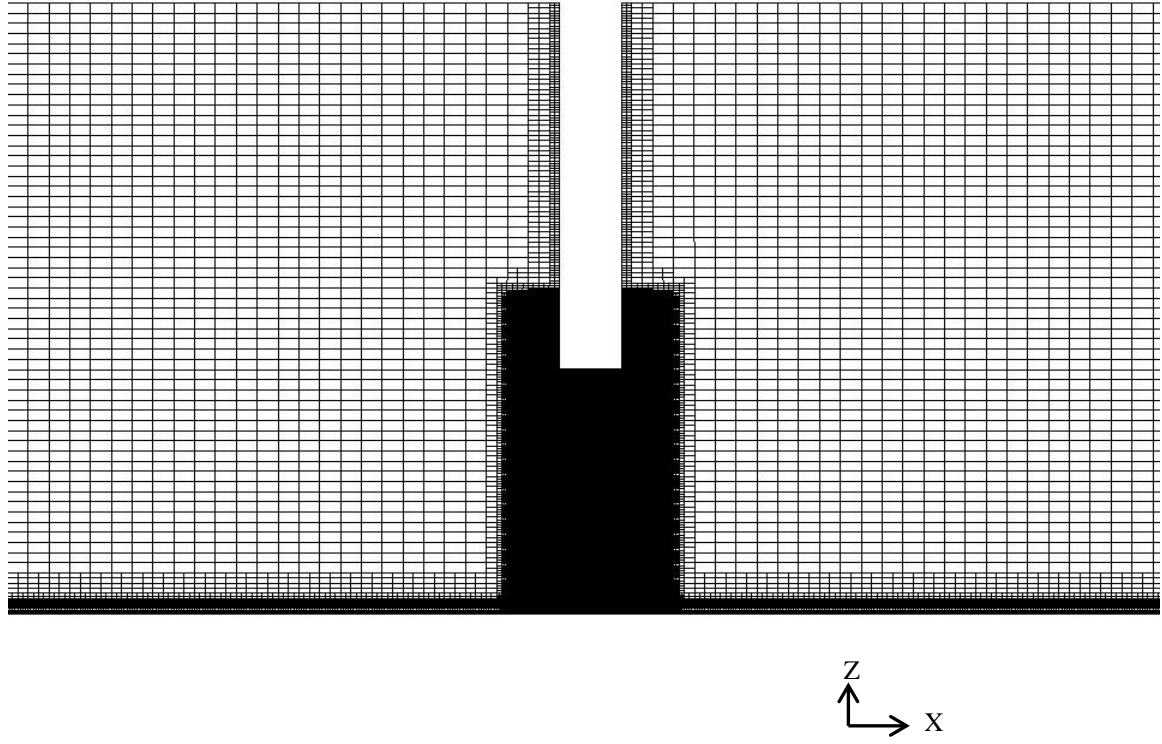


Fig. 6 Mesh of case without array

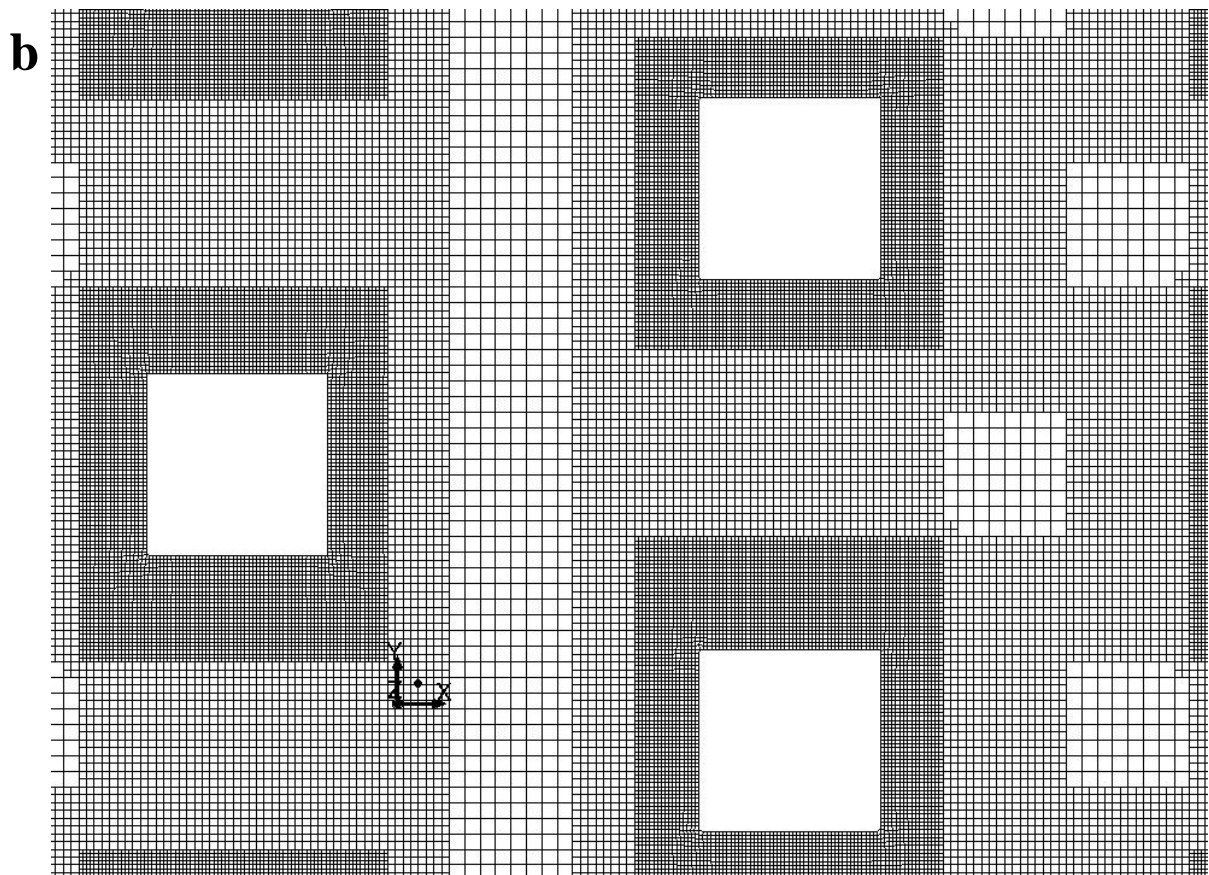
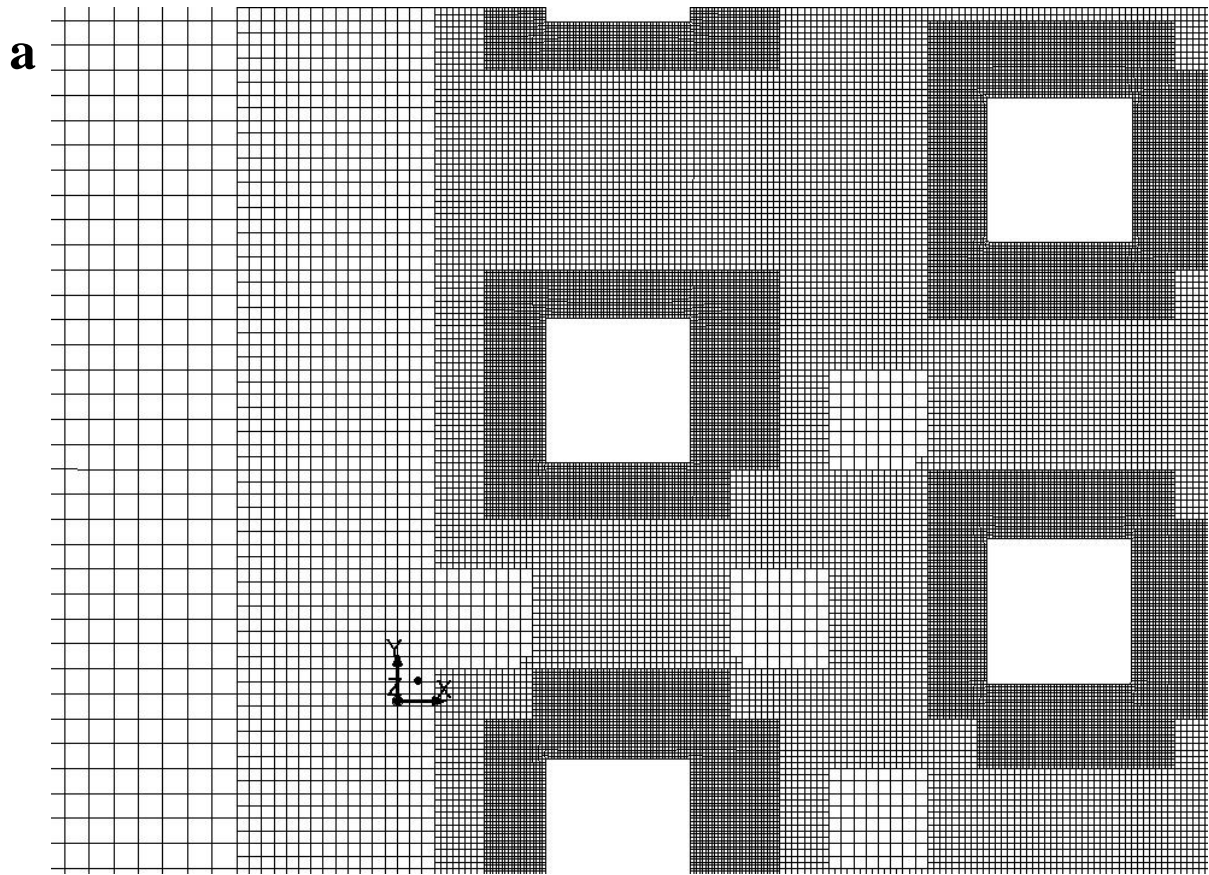
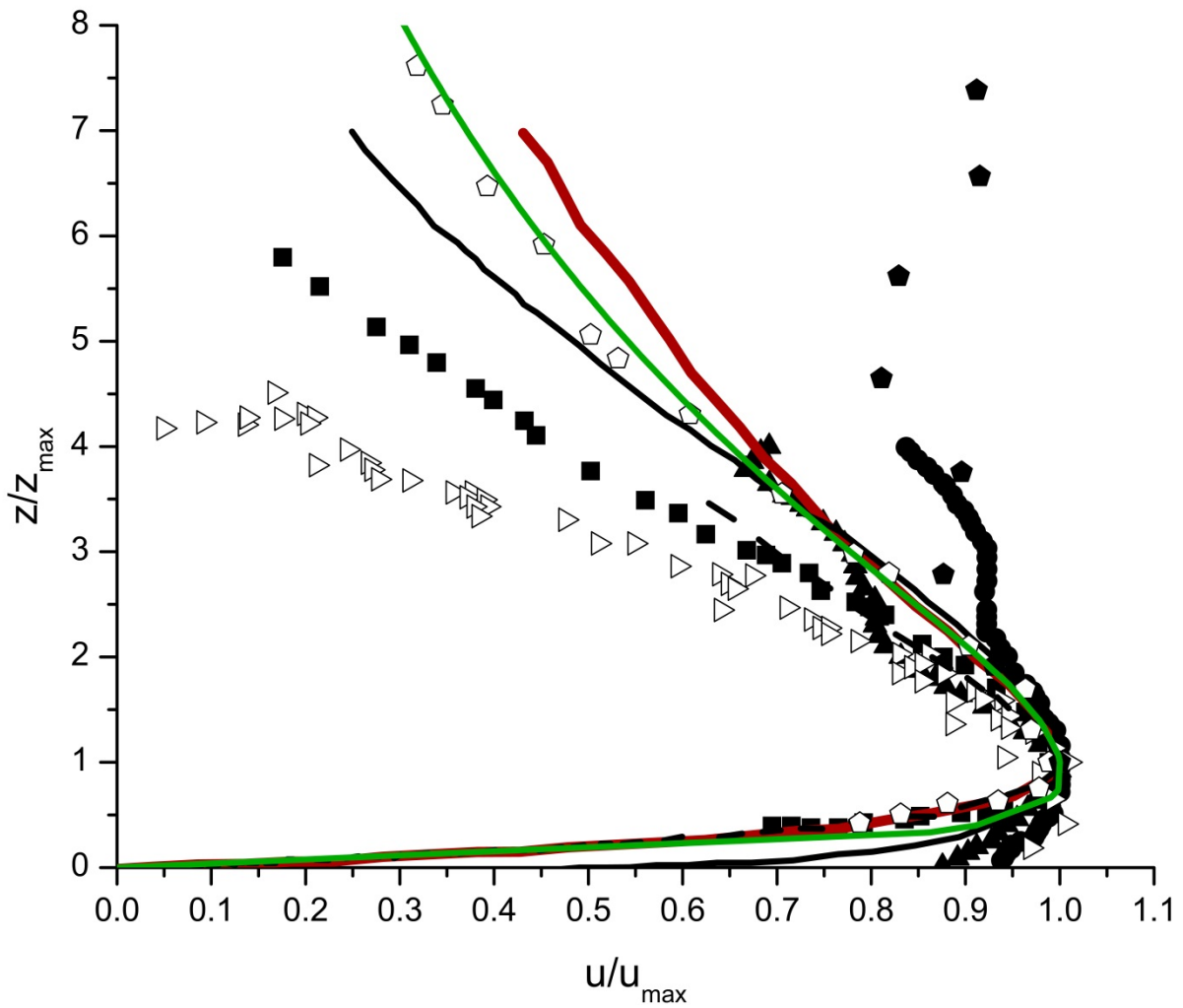


Fig. 7 Mesh for case with array S5: (a) around the upstream first two row, (b) around two intermediate rows of buildings



- Experiment (Zhang *et. al.*, 2013; $Re=2.52 \times 10^5$; $H/D=2$)
- Field - upper limit (Hjemfelt, 1988)
- ▲ Field - lower limit (Hjemfelt, 1988)
- Analytical (Oseguera & Bowles, 1988)
- Analytical (Wood *et. al.*, 2001)
- ▷ Experiment (Sengupta & Sarkar, 2008; $Re=1.39 \times 10^5$; $H/D=1.98$)
- - Analytical (Vicroy, 1991)
- Field (Fujita, 1981)
- ◆ Experiment (Mason *et. al.*, 2005; $Re=3.14 \times 10^5$; $H/D=1.7$)
- Present ($Re=2 \times 10^4$; $H/D=2$)

Fig. 8 (Color online). Time-averaged vertical profile of radial velocity from field measurements, experiments, numerical simulations and semi-empirical models at $r/D=1$.

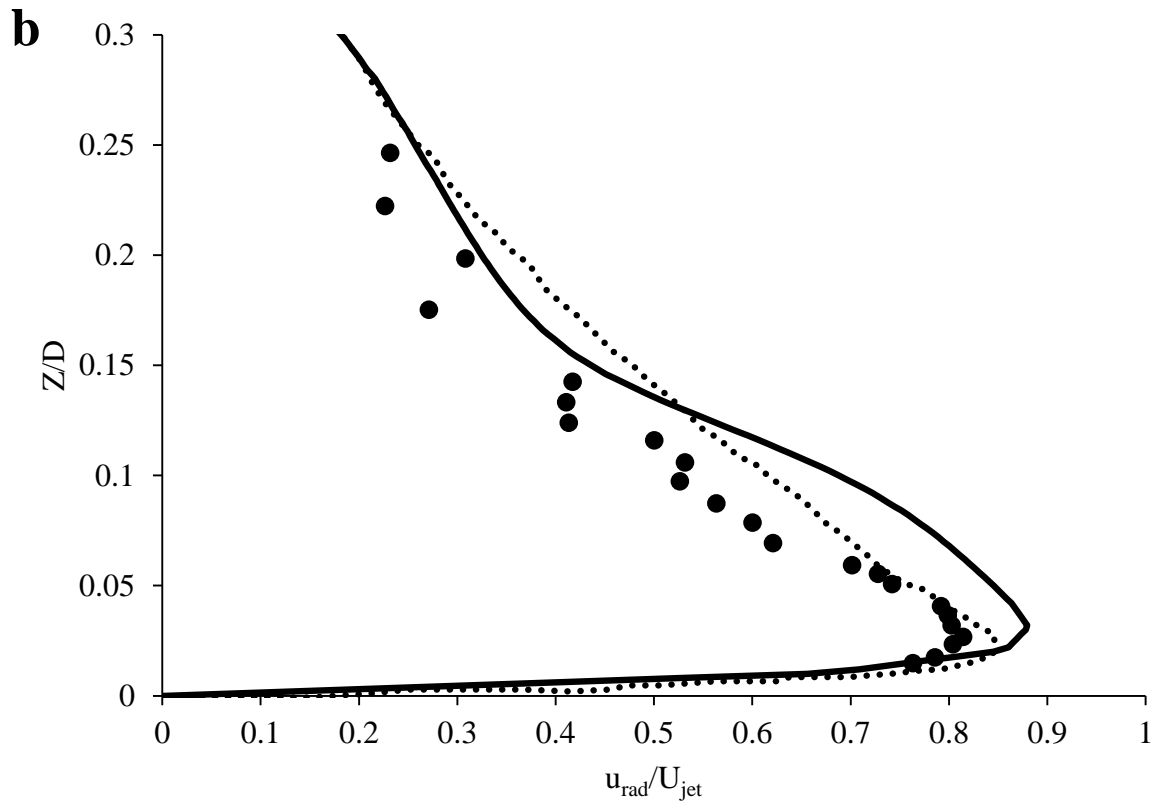
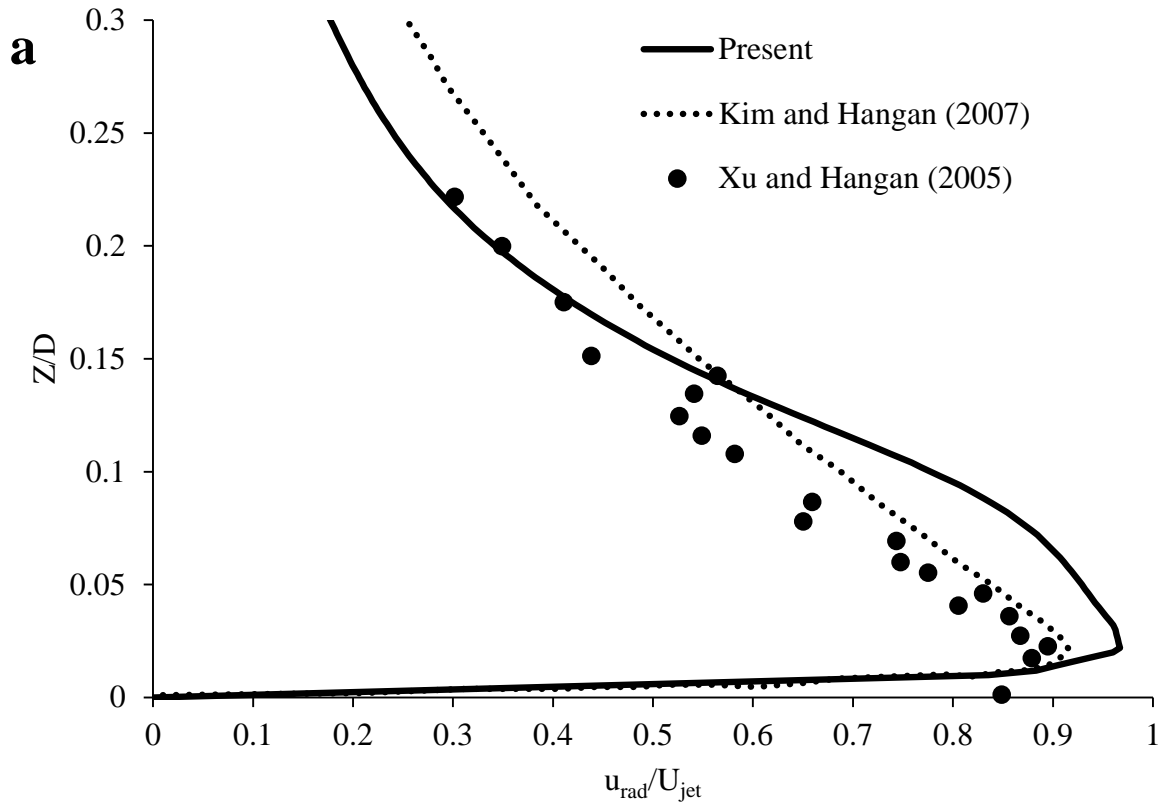


Fig. 9 Time-averaged vertical profile of radial velocity for impinging jet. (a) $r/D = 1$, (b) $r/D = 1.4$, (c) $r/D = 2.0$, and (d) $r/D = 2.5$.

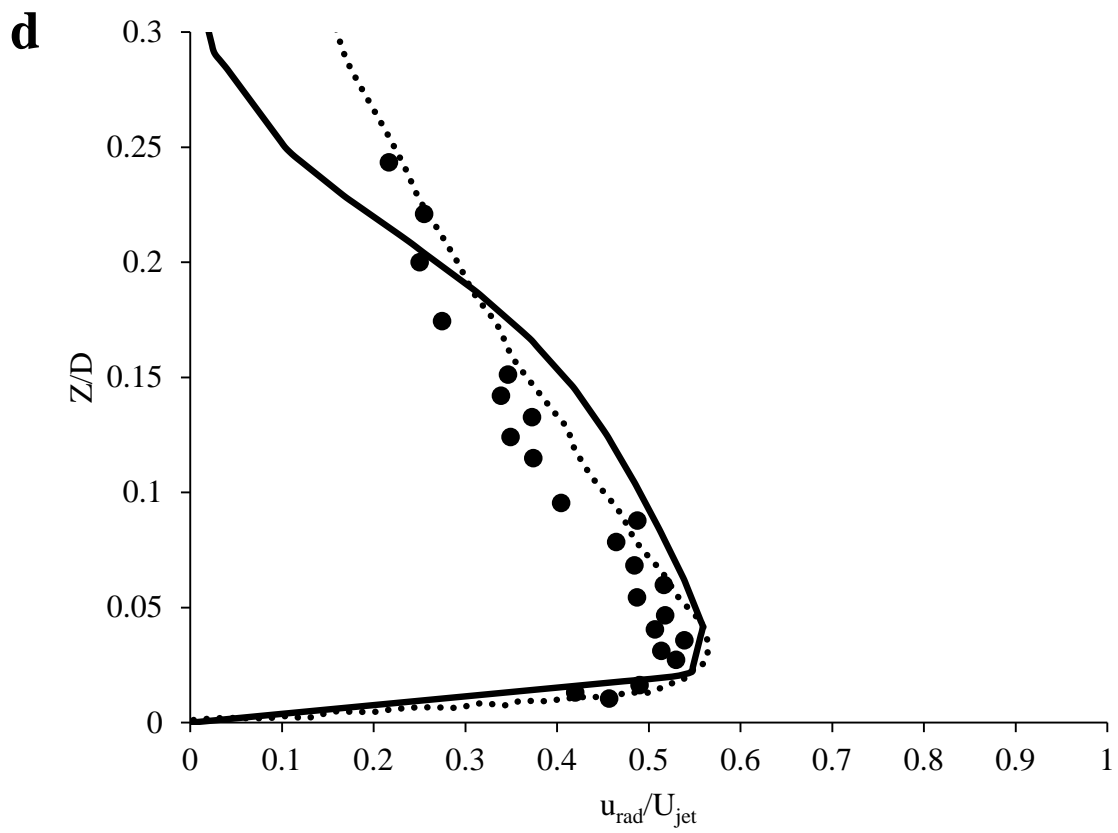
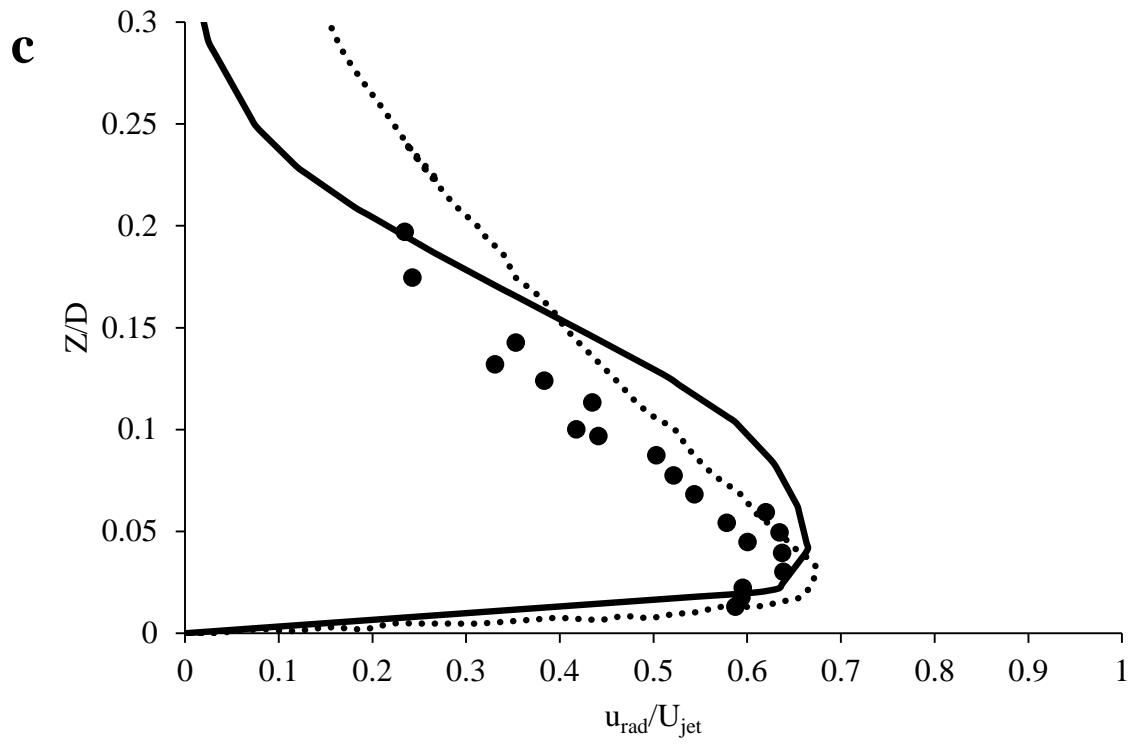


Fig. 9 Time-averaged vertical profile of radial velocity for impinging jet. (a) $r/D = 1$, (b) $r/D = 1.4$, (c) $r/D = 2.0$, and (d) $r/D = 2.5$.

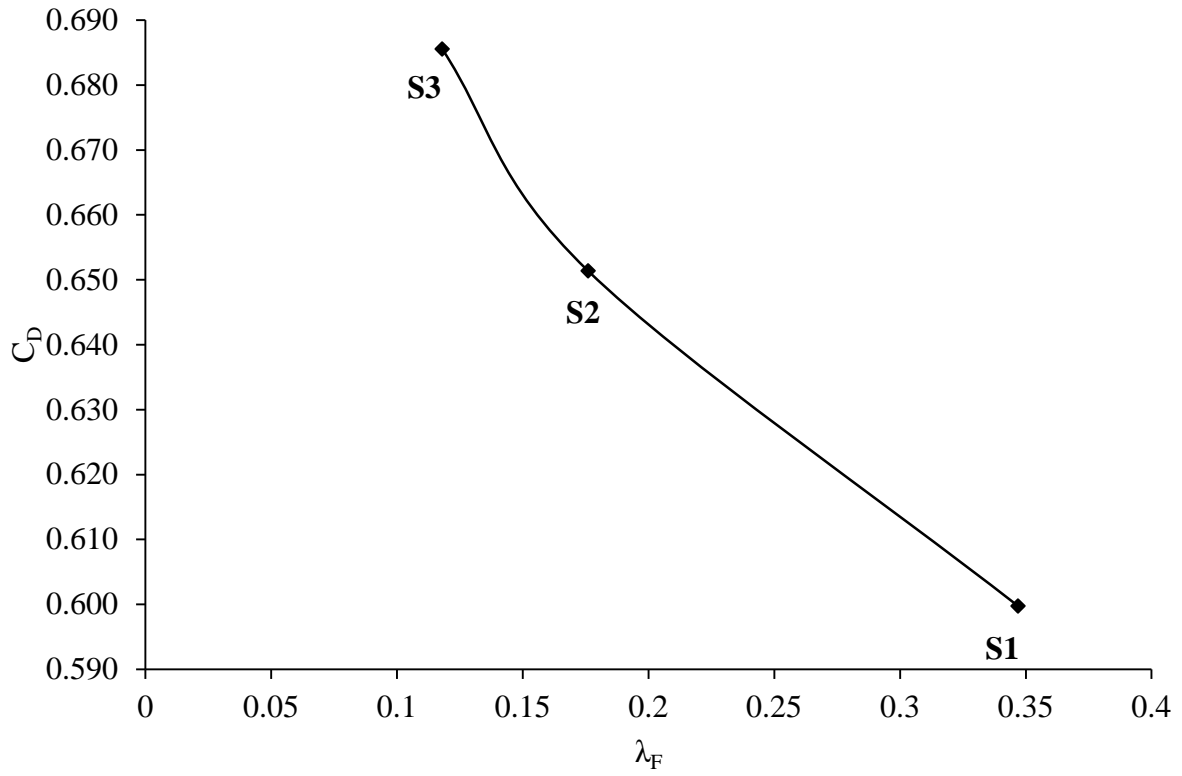


Fig. 10 Variation of time-averaged C_D with λ_F (for S1, S2 and S3)

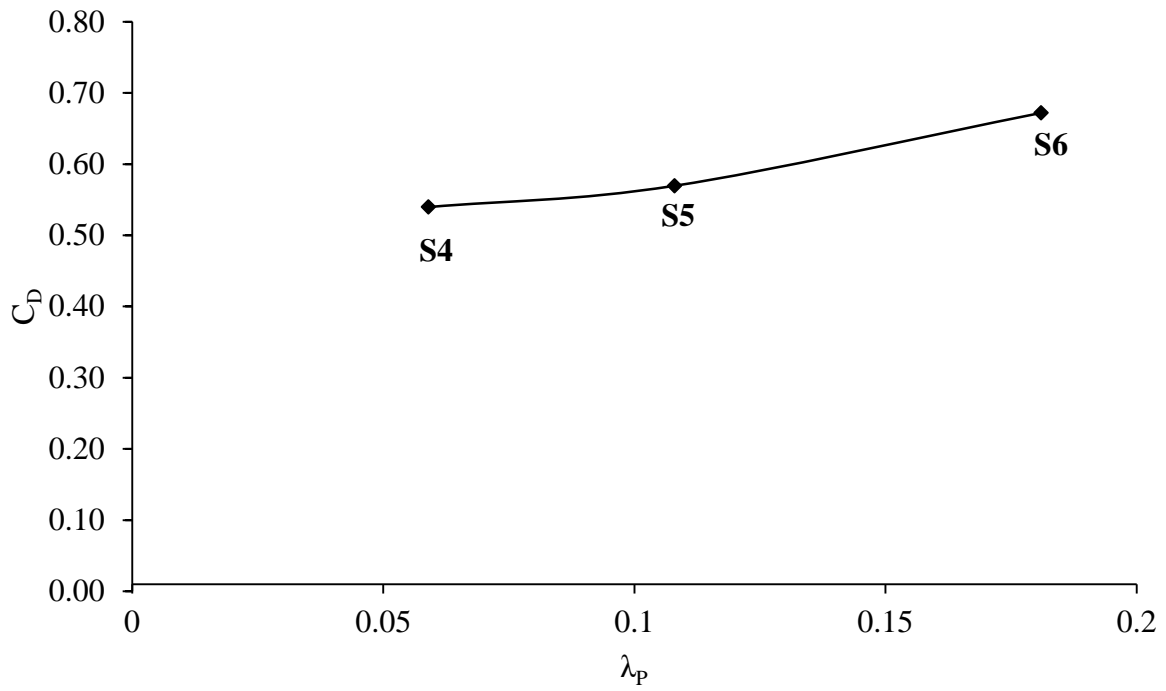


Fig. 11 Variation of time-averaged C_D with λ_P (for S4, S5, S6)

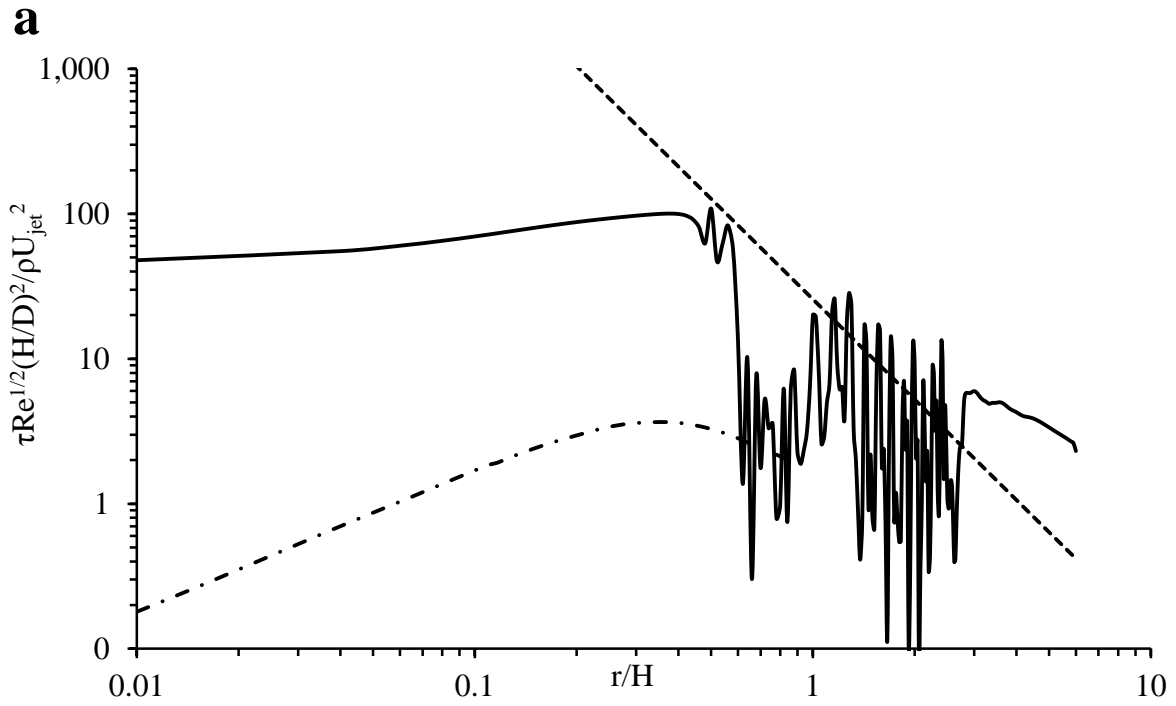


Fig. 12 Time-averaged wall shear stress along the x-axis for cases: (a) S1, (b) S4. (—) present results at $Re = 2.41 \times 10^9$ and $H/D = 2$; (- - -) Poreh *et al.* (1967 wall jet model at $Re = 2.41 \times 10^9$ (- · - ·) Phares *et al.* (2000) impingement zone model at $Re \sim O(10^4)$ and $H/D = 2$.

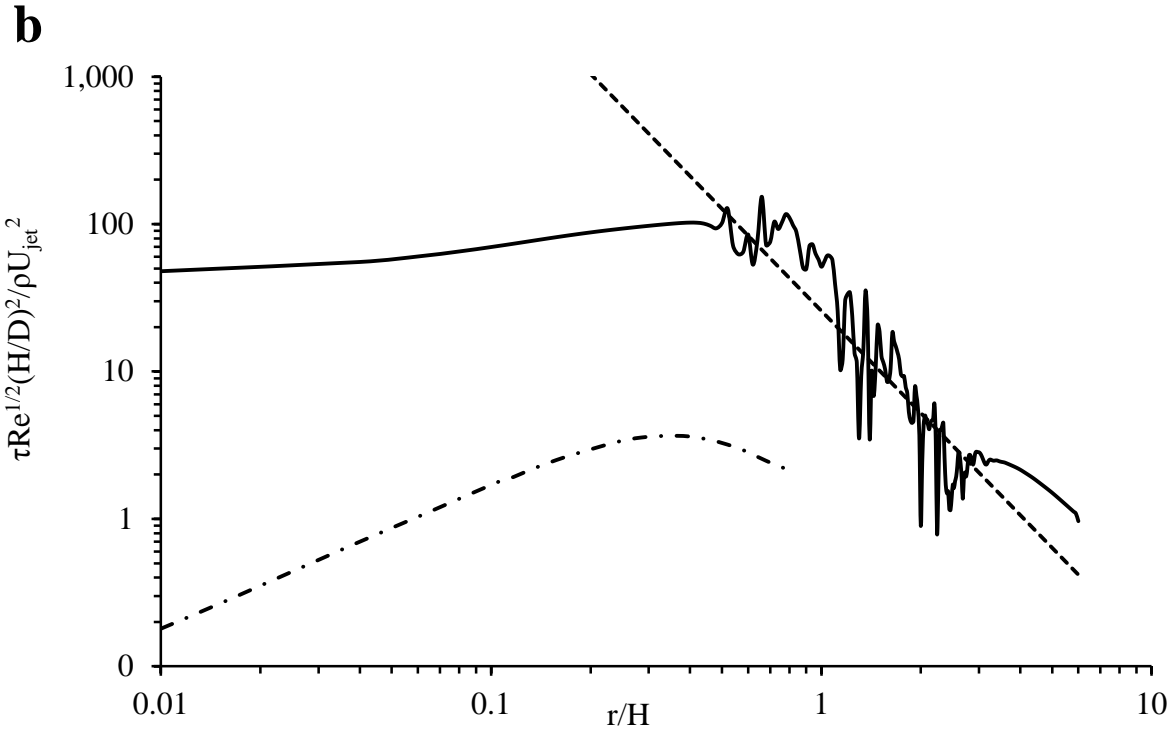


Fig. 12 Time-averaged wall shear stress along the x-axis for cases: (a) S1, (b) S4. (—) Present results at $\text{Re} = 2.41 \times 10^9$ and $H/D = 2$; (----) Poreh *et al.* (1967 wall jet model at $\text{Re} = 2.41 \times 10^9$; (- · - ·) Phares *et al.* (2000). impingement zone model at $\text{Re} \sim O(10^4)$ and $H/D = 2$.

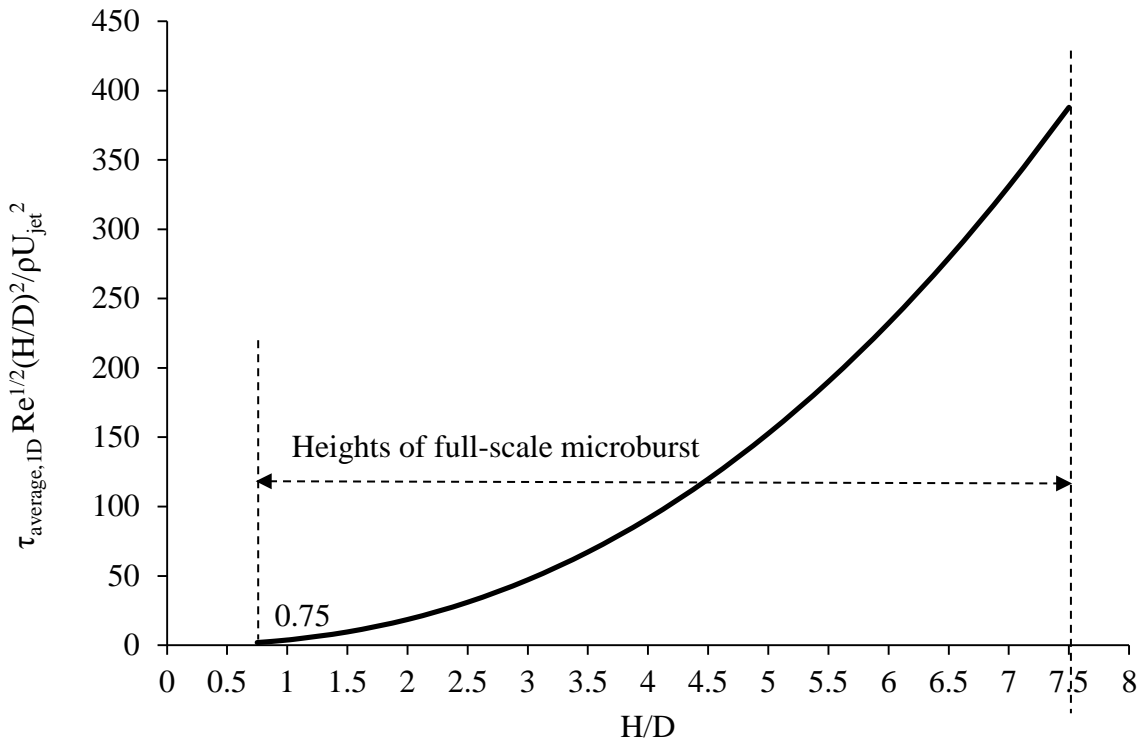


Fig. 13 Variation of spatially-averaged wall shear stress with H/D ratio along the centreline of array (U_{jet} is kept constant at 75m/s, the highest recorded speed from field measurement, D is 500m and L_s is kept to the length of the array used in the present study).

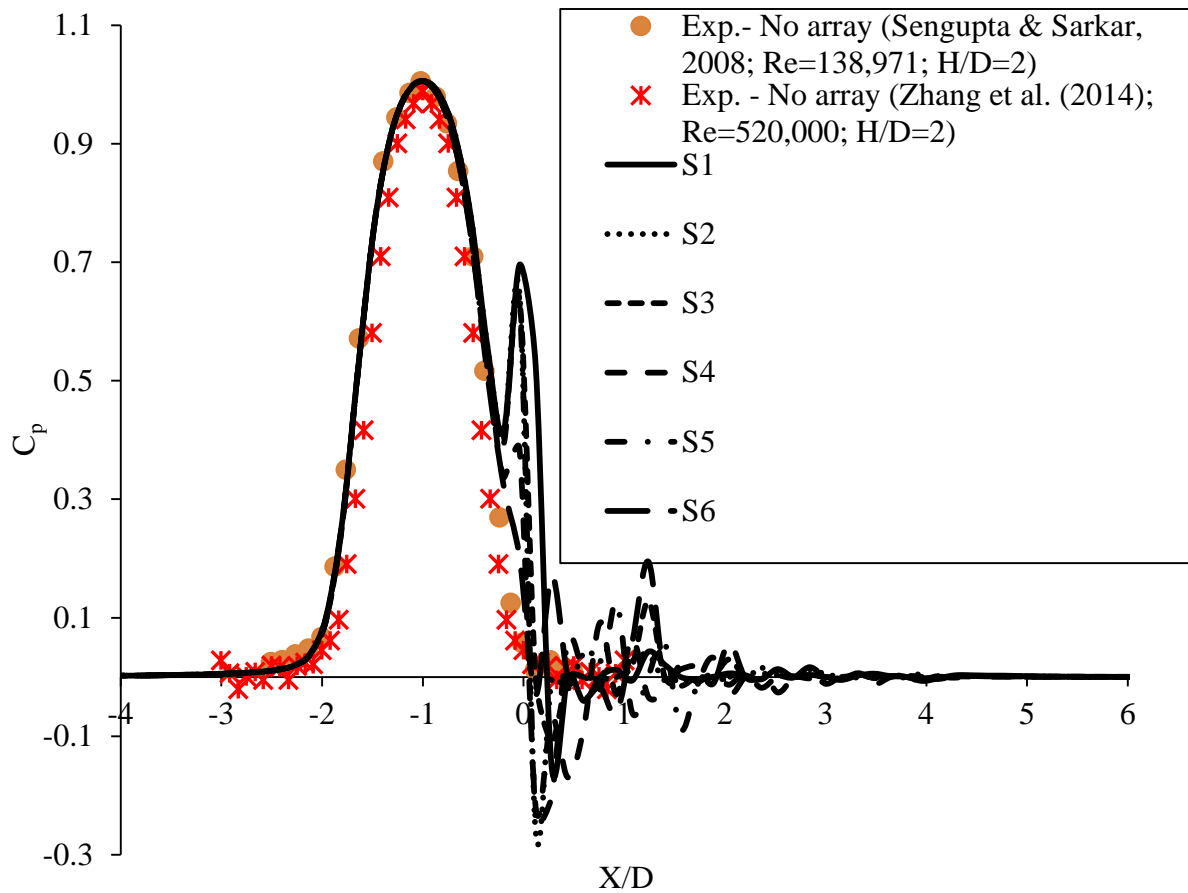


Fig. 14 Comparison of C_p along the X-axis for S1, S2, S3, S4, S5 and S6. Sengupta and Sarkar (2008), and Zhang *et. al.* (2014b) experimental results (without obstacles) are included.

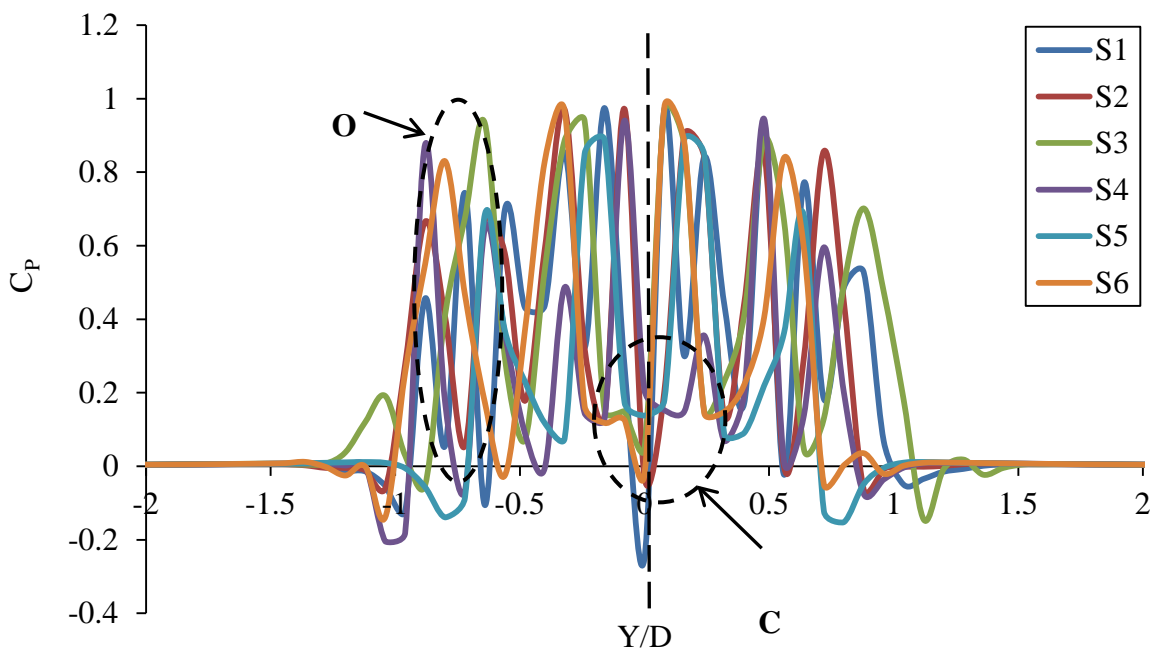


Fig. 15 (Color online). Variation of C_p along span-wise direction at $X/D = 0$.

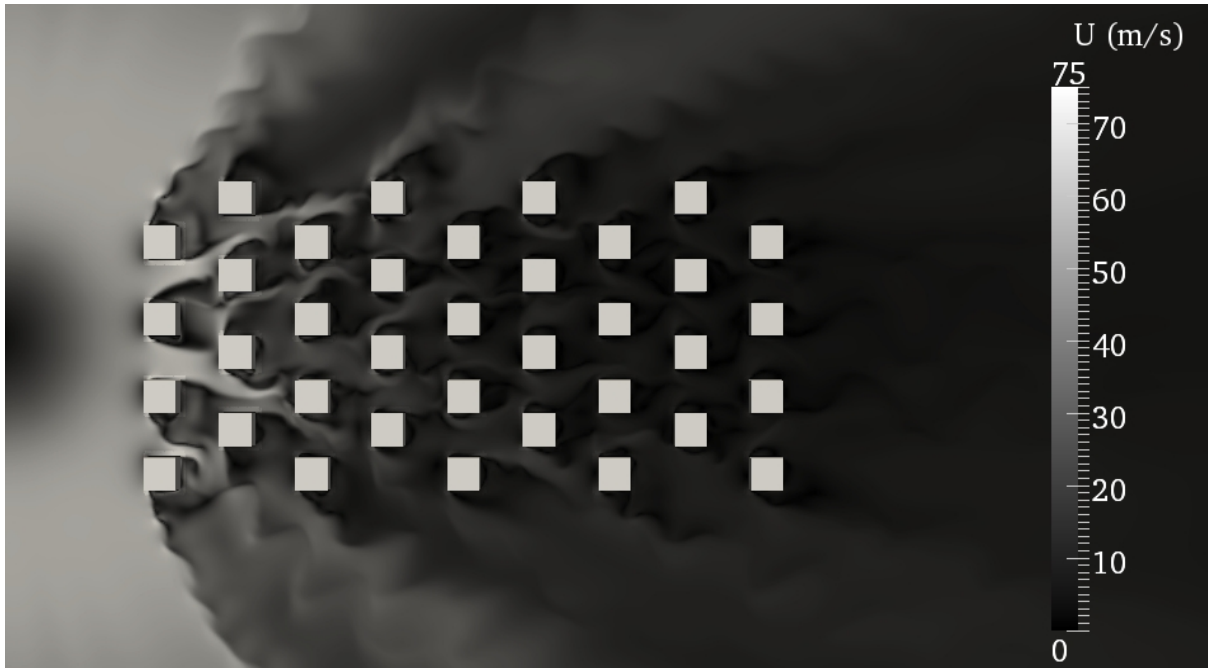


Fig. 16 The mean velocity contour plot of S6 at the level 0.5H above the ground

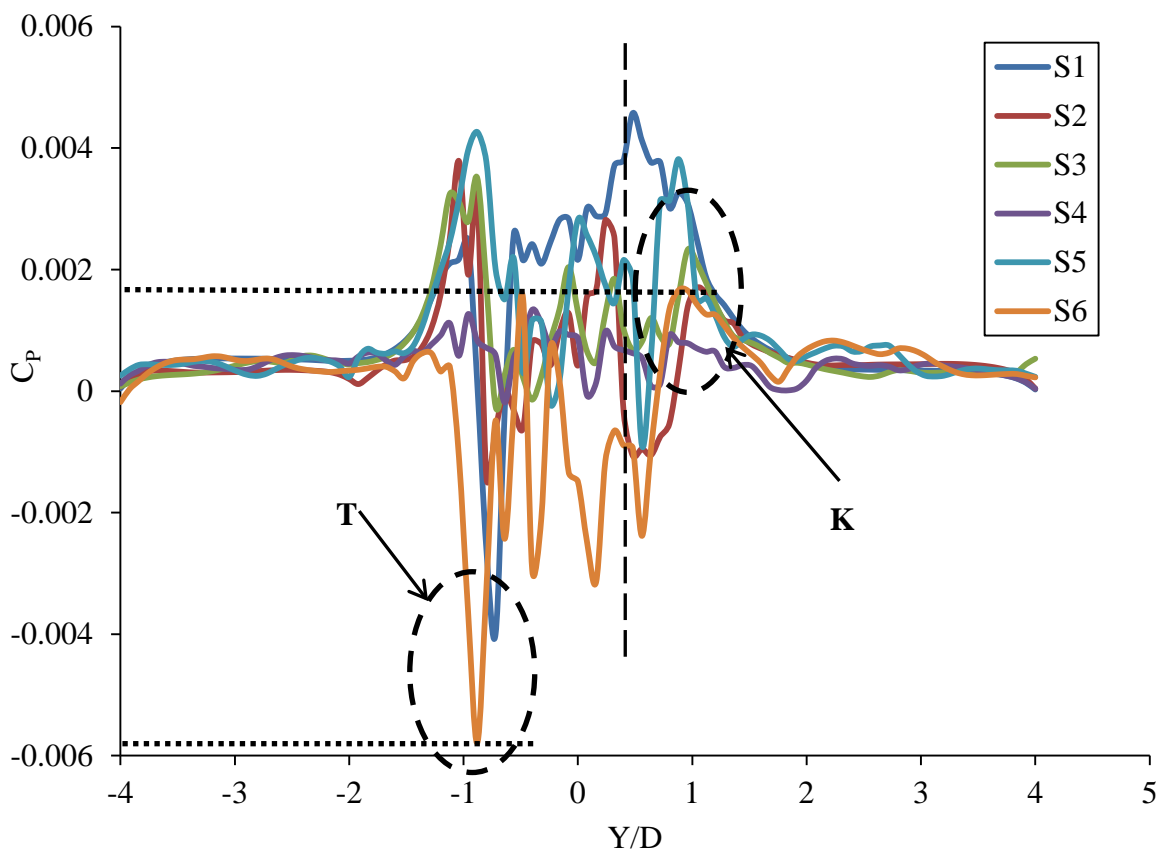


Fig. 17 (Color online). Variation of C_p along span-wise direction at $X/D = 4.68$.

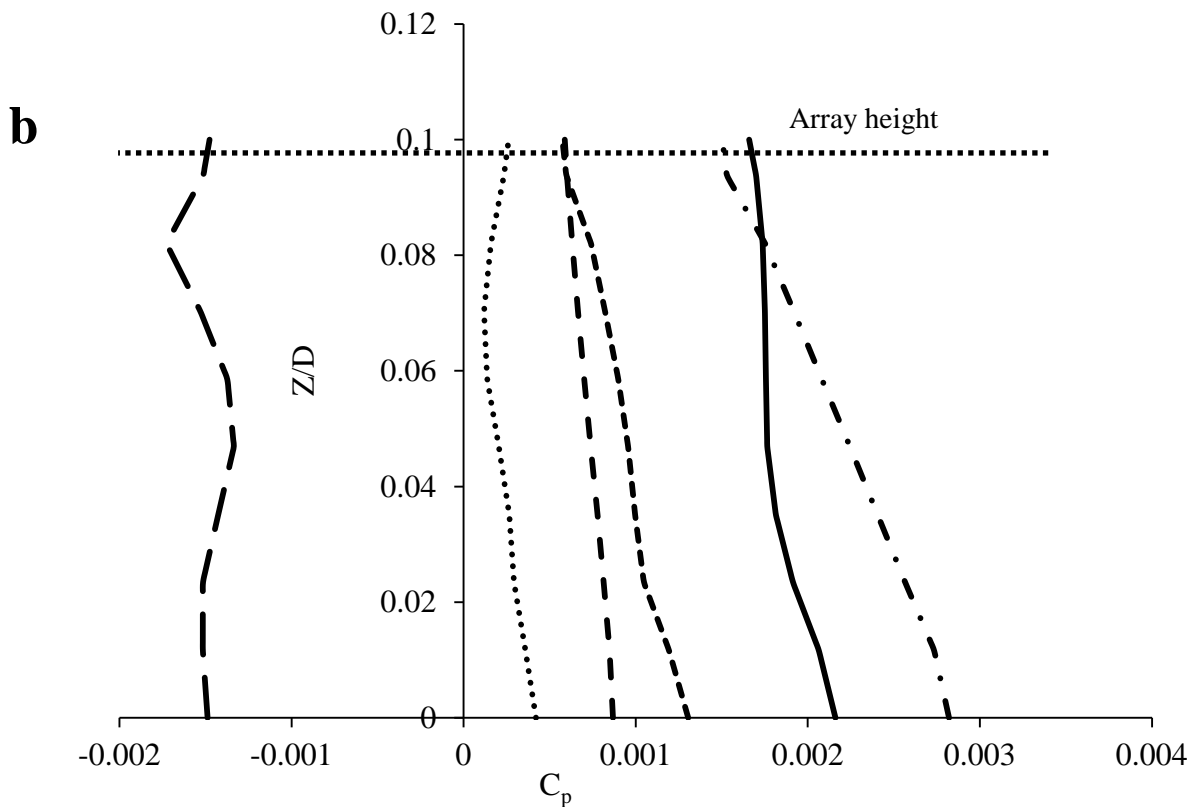
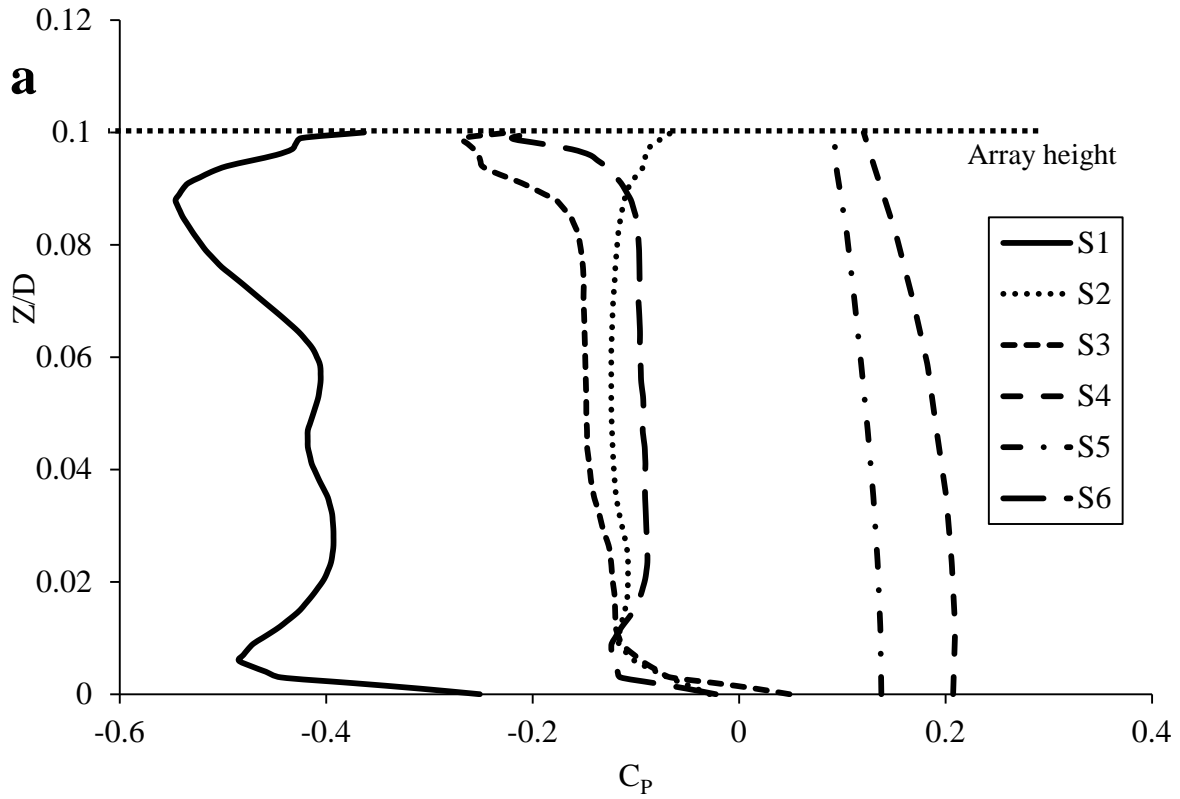


Fig. 18 Variation of C_p in vertical direction at (a) $X/D = 0$, (b) $X/D = 4.68$ on the centreline of array.

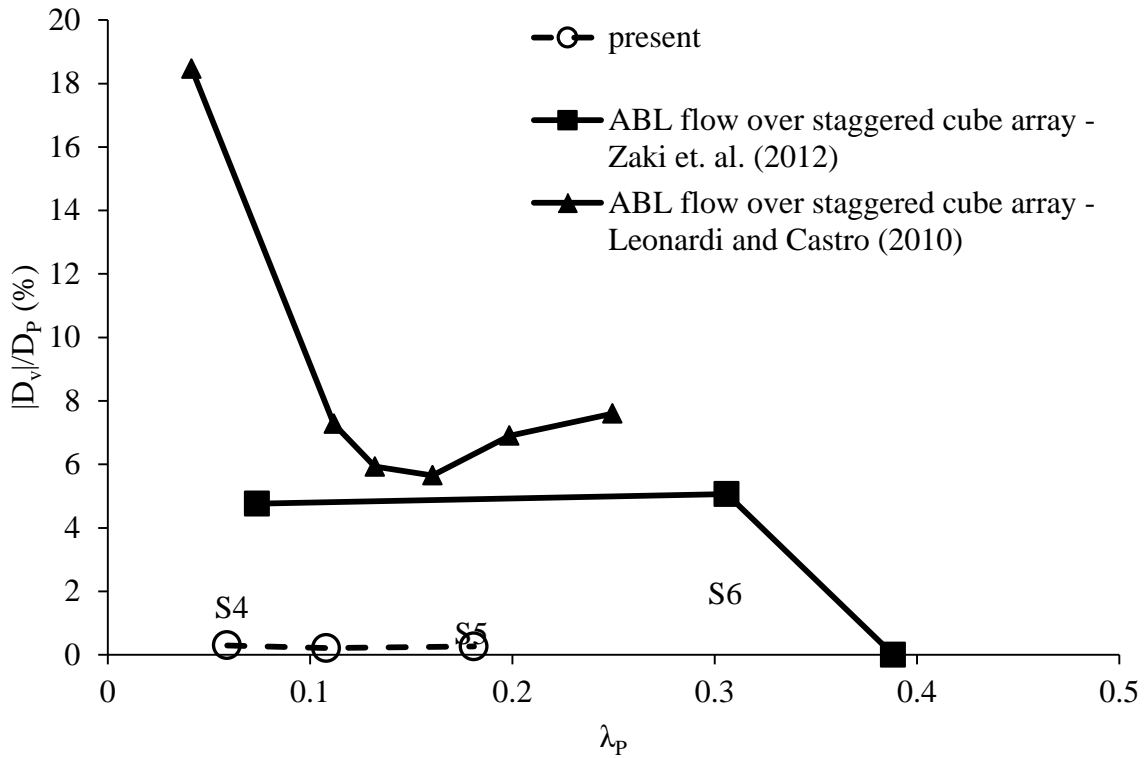


Fig. 19, D_v/D_p from the present simulation versus λ_p . Also included are: ABL flow over staggered cube array from Zaki *et. al.* (2012)'s experimental study ($Re_T \approx 2 \times 10^4$) and Leonardi and Castro (2010)'s DNS study ($Re_T = 7,000$)

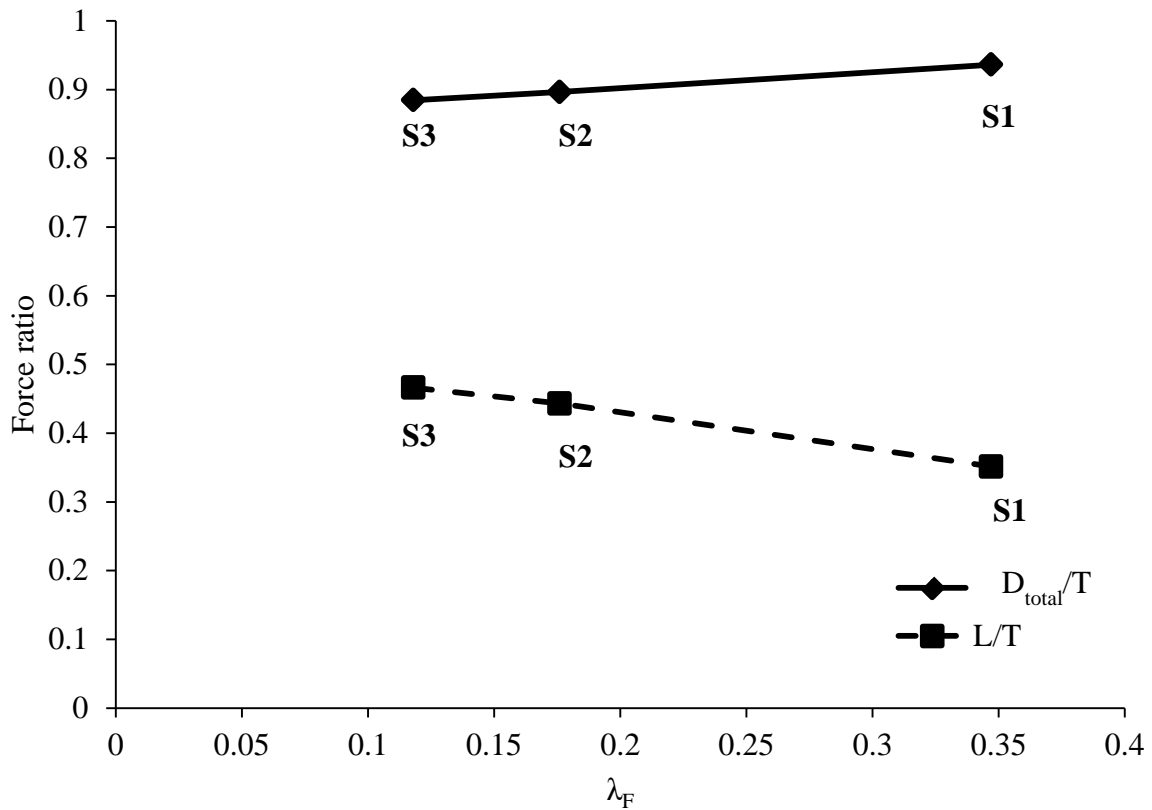


Fig. 20 Variation of L/T and D_{total}/T for various λ_F

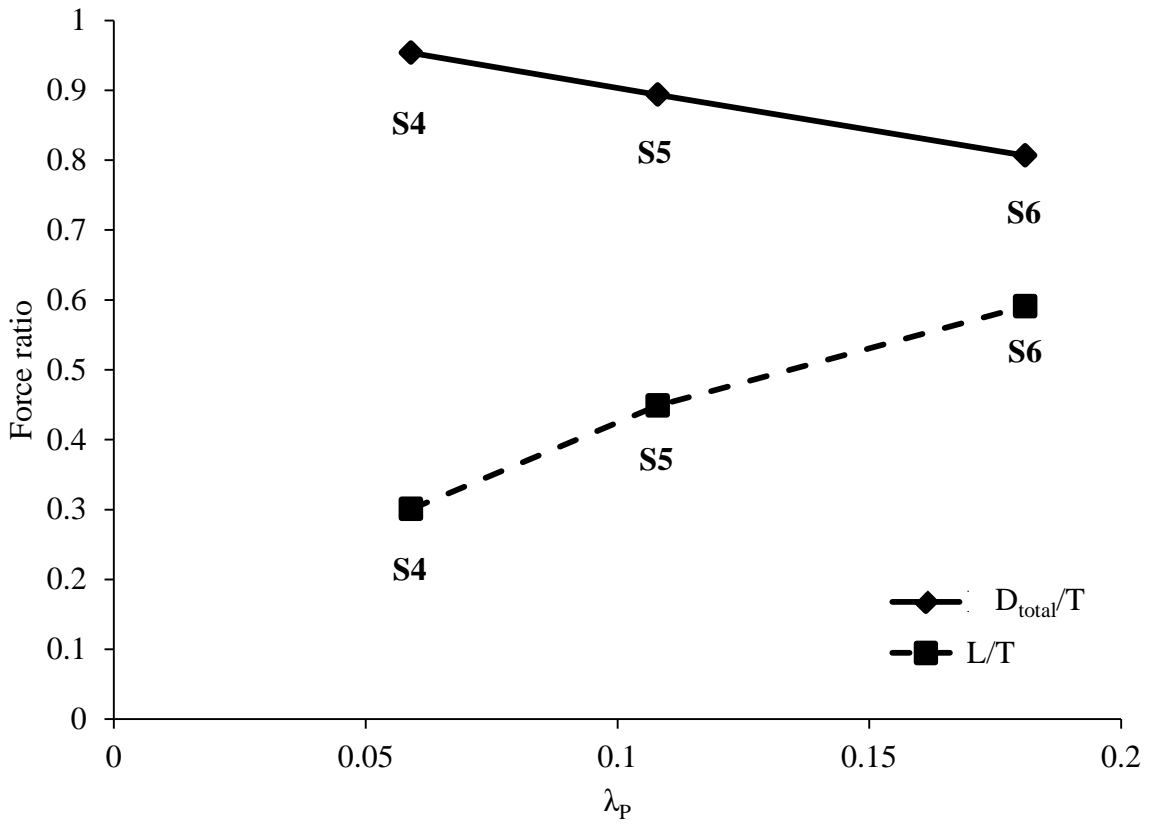


Fig. 21 Variation of L/T and D_{total}/T for various λ_p

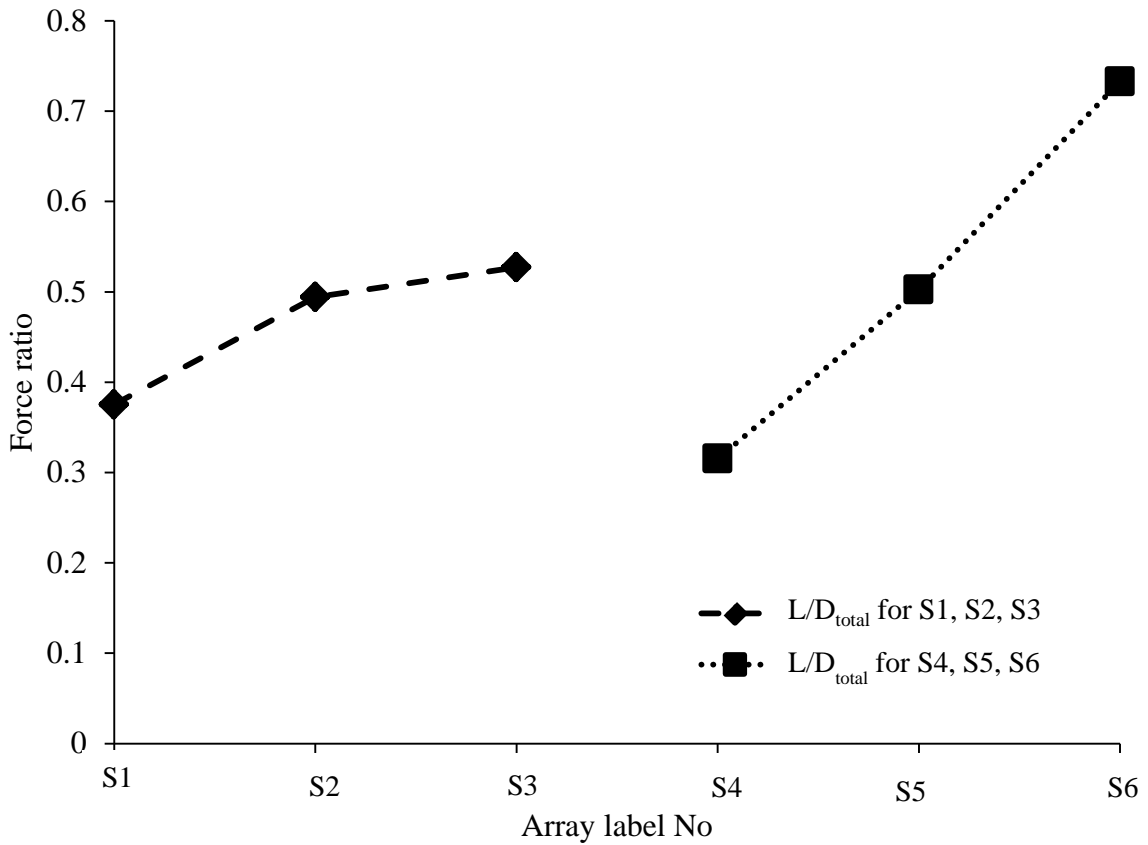


Fig. 22 Variation of L/D_{total} for various arrays